CompoHyDen: Hyperspectral Image Restoration via Nonconvex Componentwise Minimization

Hazique Aetesam [ID], Abdul Wasi [ID], and Sonal Sharma [ID]

Abstract—In this article, we propose a variational approach for estimating the clean hyperspectral images (HSI) that are corrupted by the combined effect of Gaussian noise, impulse noise, stripes, and deadlines. Successful removal of noise from the corrupted observations is essential for subsequent downstream analyses like classification, spectral unmixing, and target tracking. The main contribution of this work is as follows. *First,* an objective function is designed for the joint estimation of clean data and impulse corrupted pixels. A rationale is presented for using the ℓ_0−norm to estimate the exact sparsity induced by impulse noise. *Second,* the problem is reformulated as a multiconvex problem, which is solved using proximal projection and alternating minimization. *Third,* to exploit the spatial-spectral similarity, a nonlocal and vectorized version of total variation regularization is proposed to estimate the clean data. *Lastly*, a study on the parameter sensitivity analysis empirically validates the convergence of the restoration results under different values of the regularization hyperparameters. The experiments conducted over synthetically corrupted and real HSI data obtained from hyperspectral sensors suggest the potential utility of the proposed methodology (*CompoHyDen*) at a scalable level.

Index Terms—Alternating minimization, Gaussian-impulse noise, hyperspectral imaging, nonlocal total variation (TV), proximal projection.

I. INTRODUCTION

IMAGES acquired from traditional cameras contain a single-channel grayscale image or a combination of red, green, and blue channels for colored images. Under such acquisition settings, some of the remotely sensed data cannot capture the gamut of information beyond the visible parts of the electromagnetic spectrum from the target area under investigation [1]. Hyperspectral sensors provide an added incentive by capturing images in the wavelength range spanning 400−2500 nm [2]. The resultant hyperspectral datacube contains hundreds of spectral bands in a contiguous wavelength range. This aids in the application of hyperspectral imaging (HSI) in fields related to agriculture, food quality, remote sensing, military surveillance, and biomedicine [3], to name a few.

However, HSIs are prone to corruption during the acquisition and transmission stages. On the one hand, Gaussian noise is attributed to the thermal agitation of charge carriers and low-radiance energy captured as a result of the narrow splicing of the pixel spectrum [4]. On the other hand, impulse noise occurs when sensors go out of the radiometric range; rendering horizontal and vertical stripes in the data. Faulty memory locations and corrupted sensor elements are other factors responsible for impulse noise [5]. These are rendered as dead pixels in the acquired datacube. As a result, remotely sensed images contain a combination of Gaussian and impulse noise [6]. Noise removal is a longstanding problem and an essential prerequisite for successfully applying downstream analyses such as classification [7], spectral unmixing [8], and target tracking [9].

II. RELATED WORKS

This section provides a concise overview of the literature relevant to hyperspectral image (HSI) noise removal. Restoration of HSIs can be done using *filtering-based*, image priors [*total variation (TV)*, *low-rank*], and *learning-based* [10], [11] approaches. All these categories lack any proper boundary among them, as the amalgamation of two or more of the other categories has been explored in recent works. Further, since the scope of this article is prior-based variational technique, we do not discuss the learning-based approaches here. The following paragraphs provide a concise overview of each of the above-stated categories.

Under the filtering-based methods, Deng et al. [12] proposed a method that was basically a randomized algorithm for patch-based filtering of images. This Monte Carlo method is highly time efficient compared to other nonlocal means (NLM) methods. Aswathy et al. [13] used a sparsity-based strategy to effectively restore HSIs by employing low-pass sparse banded filter matrices. However, the main limitations of filtering-based approaches include manual tuning of hyperparameters like window size and patch-size (in NLM-based methods). Computational bottlenecks during 3-D processing of the data cannot be denied as well.

For the TV-based methods, Zhong et al. [14] quantified the sparsity of deadlines, stripes, and other noise sources by employing the nonconvex and nonsmooth ℓ_0−norm, restoring hyperspectral images with high accuracy. Kong et al. [15] presented a group of low-rank and spatial-spectral TV for image restoration. It meticulously extracts spatial information while removing Gaussian and sparse noise too. In another approach, Wang et al. [16] proposed ℓ_0 TV along with tensor low-rank

constraint for hyperspectral image noise removal, claiming that it preserves more information than ℓ_1 norm for further processing. Peng et al. [17] proposed an optimized 3-D TV regularizer that captured sparsity along all gradient maps of an HSI and reflected correlation among all these bands. This helps in better processing of these images. Wang et al. [18] argued that TV-based methods introduce artifacts by oversmoothing the image. To circumvent this, their proposed model exploits the spatial-spectral information both locally and globally, showing better edge preservation capability.

In low-rank based methods, Zhuang et al. [19] exploited the properties of self-similarity and low dimensionality to produce a model exhibiting insensitivity to its parameters to denoise hyperspectral images. Mahmood and Sears [20] proposed a model that helps in the estimation of noise at each pixel of a hyperspectral image without divulging any information about the statistical nature of noise. They emphasized that it could also aid in image noise removal when it exhibited spectral correlation. For hyperspectral images that are corrupted by a combination of stripe, Gaussian, and impulse noises, Jiang et al. [21] proposed a method that exploited expectation maximization for restoration while working on low-rank and self-similarity. Chen et al. [22] pointed out that a large amount of work was done on HSI denoising based on the independent and identically distributed (iid) nature of noise. Therefore, they proposed a model in the Bayesian framework that adapted to tackle various noises that are non-iid in nature. Pertinent to mention is that prior-based methods require hand-crafted regularization terms for every dataset that deviates from the diverse and complex noise encountered in real HSIs.

All the preceding methods suffer from one or more deficiencies.

1) ℓ_0-norm over the sparse noise component [14] and over TV regularization [16] are both nonconvex problems. They are difficult to solve and generate nonunique solutions.
2) 3-DTV involved in exploiting the texture information [15] is suboptimal in restoring Gaussian corrupted pixels mixed with sparse impulse noise. Both these noise types need different mathematical treatments. Further, low-rank determination using Tucker decomposition fails to decompose higher order tensors since they explicitly materialize intermediate data, whose size grows rapidly as order increases (≥ 3).
3) In Peng et al. [17], the nonlocal nature of image smoothness renders the method inapplicable for 3-D tensor data. Estimation of noise sparsity on subspace bases still does not handle the nonlocal nature of noise and image smoothness.
4) Since the alternating direction method of multipliers (ADMM) is inherently suited for nonsmooth convex optimization problem, its application for solving $\ell_0 - \ell_1$ hybrid TV leads to suboptimal results [18].
5) Low-rank tensor decomposition performed by singular value decomposition (SVD) in [19] is computationally intensive, specifically for data of this magnitude (dimension ≥ 3).

6) Per-pixel noise estimation [20] ignoring the statistical nature of noise leads to overestimation/underestimation of decoupled Gaussian and impulse noise corrupted pixels present in the HSI datacube. Noise estimation considering the interband correlation without the underlying assumption of noise characteristics leads to insufficient removal of high-magnitude impulse noise.
7) Gaussian mixture model (GMM) to handle the nonidentical and independently distributed (non-iid) noise in [22] is highly sensitive to the initial values of the model parameters, especially in HSI data, where there are too many components in the mixture. Further, GMM can be computationally expensive to fit on high dimensional data (≥ 3). The initial assumption under GMM is that the data comes from a mixture of normal distributions. However, the high spikes introduced by impulse corrupted pixels deviate from Gaussian distribution and more suitably follow the Laplacian scale mixture model.

Inspired by the recent developments, we aim to overcome the above stated limitations. Following are the main contributions of our work.

1) GMM used to fit mixed Gaussian-impulse noise in [22] leads to suboptimal restoration results. Therefore, in our work, the two noise sources are modeled separately using Gaussian (for Gaussian noise) and Laplace (for impulse noise) distribution. An objective function is designed for the joint estimation of clean data and impulse corrupted pixels.
2) Contrary to the work in [14], to handle the nonconvex ℓ_0-norm term, the resultant optimization problem is reformulated as a multiconvex problem involving the estimation of true clean image as well as the binary mask. To support the above argument, a rationale is presented for using ℓ_0-norm to estimate the exact sparsity induced by impulse noise. Since the resultant optimization problem is multiconvex, it can be easily solved using proximal projection and alternating minimization.
3) In the previous works [14], [15], [16], similarity weights were computed across all bands but nonlocal TV (NLTV) was computed separately for each band. This misses the interband coupling. To circumvent this difficulty, we have incorporated interband coupling by introducing a matrix K. Formally, we introduce $\ell_{\infty,1,1}-$norm in the regularization term because interchannel coupling is more in $\ell_\infty-$norm than in ℓ_2- or ℓ_1-norm.
4) A theoretical study of the convergence analysis of the proposed objective function aids in the componentwise minimization of the criterion function.

III. PRELIMINARIES AND OBJECTIVE

For an image corrupted by mixed Gaussian-impulse noise, the image formation model [23], [24] is given by

$$f_{ij} = \begin{cases} u_{ij} + g_{ij} & \forall (i,j) \in \Omega_g \\ v_{ij} & \forall (i,j) \in \Omega_s = \Omega - \Omega_g \end{cases} \tag{1}$$

where the original data u are corrupted by the Gaussian noise component $g \sim \mathcal{N}(0, \sigma_g^2)$, approximated as normal distribution with mean $\mu_g = 0$ and variance σ_g^2. $v \sim \mathcal{L}(0, \sigma_s)$ is the impulse noise component, approximated as a Laplace distribution [25] with $\mu_s = 0$ as the location parameter and σ_s as the scaling parameter. The cumulative effect of the two random variables g and v produces the composite noisy signal f. The indices (i, j) denote the pixel locations along the spatial and spectral dimensions[1]. Ω denotes the total set of pixels present in the image. Ω_g and Ω_s are the sets of Gaussian and impulse noise corrupted pixels,[2] respectively. If $\Omega_s = \emptyset$, the image is corrupted by only Gaussian noise, and the image formation model is modified as $f = u + g$. For an image corrupted by both Gaussian and impulse noise, the image formation model [26], [27] can be simplified as

$$f = u + g + v. \tag{2}$$

The optimization problem that we seek to address is given by

$$\arg\min_{u,v} \mathcal{L}(u, v) = \frac{1}{2}\|f - u - v\|_2^2 + \lambda_1 J(u) + \lambda_2 \|v\|_0 \tag{3}$$

where the first term is the data fidelity term [29], [30] in ℓ_2-norm ($\|\cdot\|_2^2$) addressing the Gaussian noise component, $J(u)$ is the regularization term over the clean data (details presented in Section IV-E), and ℓ_0-term ($\|\cdot\|_0$) models the exact sparsity of the impulse corrupted pixels. The hyperparameters λ_1 and λ_2 are adjusted based on the level of Gaussian and impulse noise, respectively.

The main objective of this article is as follows. *First*, we present the rationale behind choosing the nonconvex and noncontinuous ℓ_0-norm as the penalty term in the objective function by subsuming the variable v present in the fidelity term (Section IV-A). *Second*, to handle the difficulty introduced by ℓ_0 term, we reformulate the objective function as a multiconvex problem that is continuous (Section IV-B). *Third*, a componentwise minimization strategy is devised to solve the resultant minimization problem (Section IV-C). *Lastly*, we study the convergence of the proposed scheme based on alternating minimization and estimate the local minima by making a trivial change in the objective function (Section IV-D).

IV. PROPOSED METHODOLOGY

Since we are mainly interested in the estimation of the actual signal u, v can be eliminated from the objective function of (3) such that

$$\arg\min_u E(u) = \arg\min_v \mathcal{L}(u, v). \tag{4}$$

The resultant objective function is still nonconvex in nature. In order to solve (4), it can be written as a multiconvex problem

---

[1]It is to be noted that the original dimension of 3-D HSI data is $\mathbb{R}^{m \times n \times p}$; however to exploit the spatial-spectral similarity in the data, the 3-D matrix is converted into its corresponding Casorati matrix representation [28] such that $\{f, u, g, v\} \in \mathbb{R}^{mn \times p}$ and $\{f, u, g, v\}_{i,j} \in \mathbb{R}^{mn \times 1}$. The indices are dropped from further consideration to enhance clarity.

[2]There is a dichotomy of pixels into Gaussian and impulse corrupted ones. A pixel successively corrupted by Gaussian and later by impulse noise does not possess any information about the clean data or Gaussian corrupted pixels.
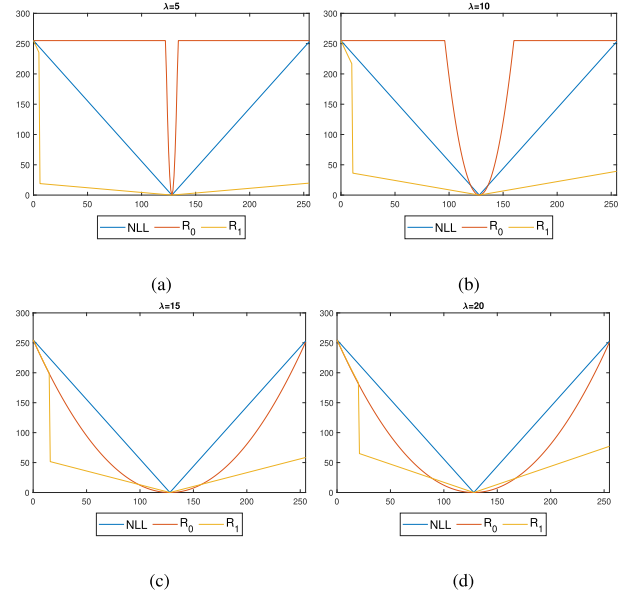

Fig. 1. Negative log-likelihood for mixed Gaussian impulse noise and its approximation using R_0 and R_1 regularizers under different values of λ. (a) $\lambda = 5$, (b) $\lambda = 10$, (c) $\lambda = 15$, and (d) $\lambda = 20$.

involving the estimation of u and the auxiliary variable Φ (more about Φ is presented in Section IV-B).

A. ℓ_0-norm as the Penalty Term

In this section, we discuss the intuition behind using ℓ_0-norm over the impulse noise component v to measure the exact sparsity of the signal. Let us consider that the function R_p is introduced over the data fidelity term to remove the component v. The resultant objective function is given by

$$E^p(u) = \frac{1}{2} R_p \|f - u\| + \lambda_1 J(u). \tag{5}$$

Based on whether ℓ_0- or ℓ_1-norm is a better choice to approximate impulse noise, pixelwise R_0 and R_1 (for $p = 0$ and $p = 1$, respectively) is given by

$$R_0(x) = \min(|x|^2, 2\lambda_2) \tag{6a}$$

$$R_1(x) = \begin{cases} |x|^2 & \text{;if } |x| \leq \lambda_2 \\ 2\lambda_2|x| - \lambda_2^2 & \text{;otherwise.} \end{cases} \tag{6b}$$

The fidelity term $\frac{1}{2}R_p\|f - u\|$ in (5) approximates the negative log-likelihood under mixed Gaussian-impulse noise based on the value of p in R_p. Fig. 1 is used to simulate the negative log-likelihood of R_1 and R_0 for a pixel whose original intensity level is 128. It is initially corrupted by Gaussian noise of specific level (here, $\sigma = 10$) followed by random-valued impulse noise (RVIN) (considering that the dynamic range of the data is $[0, 255]$) [31]. The experiment is simulated for 10^{10} iterations. There are several observations that can be made here. *First*, R_1 possesses somewhat erratic behavior as it is evident from the figures that it is quite different from the negative log-likelihood (indicated by the blue color). It can be observed from
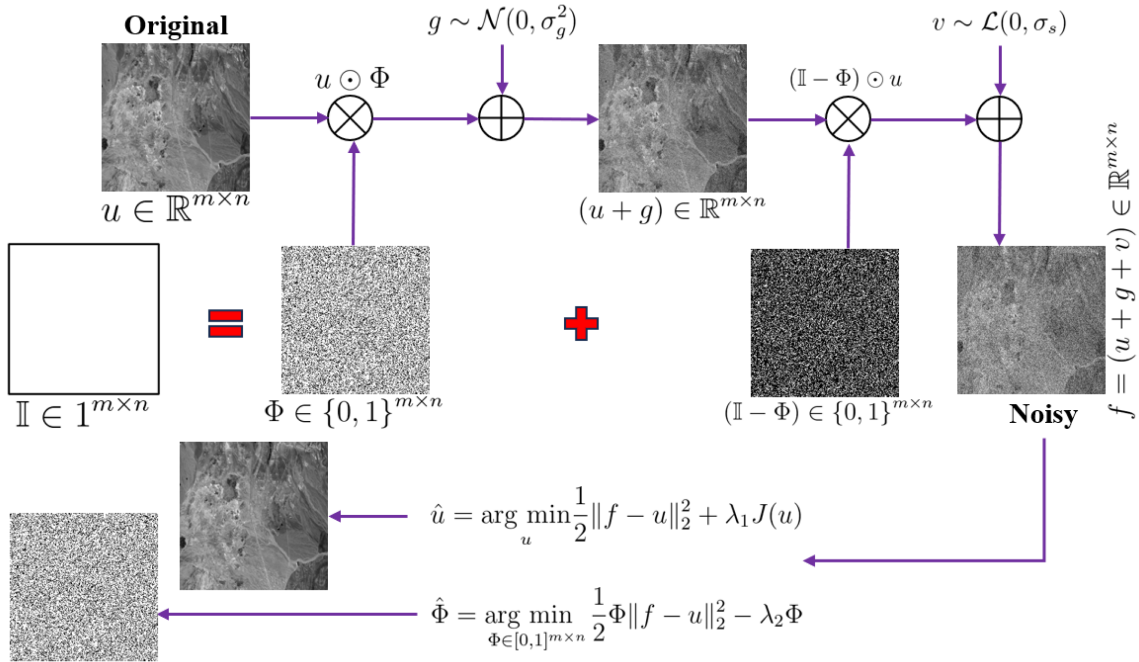
Fig. 2. Proposed HSI denoising model: *CompoHyDen*. $\otimes$ is used to denote the Hadamard product while $\oplus$ represents the additive nature of the two noise sources (g, v).

the figure that the graph for R_0 better approximates the negative log-likelihood than the R_1 term. *Second,* R_1 is highly sensitive to the values of the hyperparameter λ_2 [see Fig. 1(a)–(c)]. *Lastly,* for higher values of $\lambda_2 = \{15, 20\}$, the performance saturates for both R_0 and R_1. Conclusively, we can state that R_0 is more robust to the value of the hyperparameter λ_2, and thus, ℓ_0-norm in the penalty term is a more suitable choice to model the exact sparsity of the impulse corrupted pixels.

B. Multiconvex Problem

Now that we are equipped with the knowledge that ℓ_0-norm is a more suitable choice as the penalty term to model the exact sparsity of impulse noise, we next introduce an auxiliary variable defined by

$$\Phi_{i,j} = \begin{cases} 0; \text{ if } v_{i,j} \neq 0 \\ 1; \text{ if } v_{i,j} = 0 \end{cases} \quad (7)$$

where $\Phi_{i,j}$ is a binary matrix[3] having the same dimension as u. To handle the nonconvex ℓ_0-term in our objective function, (3) can be modified as a multiconvex problem

$$\arg\min_{u, \Phi \in \{0,1\}} \mathcal{L}(u, \Phi) = \frac{1}{2}\Phi\|f - u\|_2^2 + \lambda_1 J(u) + \lambda_2(\mathbb{I} - \Phi) \quad (8)$$

where $\mathbb{I} \in \mathbb{1}^{mn \times p}$ and the term $(\mathbb{I} - \Phi)$ is used to approximate the ℓ_0 term. $\mathbb{I}$ is the matrix with all ones. Since Φ is a binary matrix, it acts as a mask over the input image u to decouple the effect of Gaussian and impulse noise (see Fig. 2 for more details).

---

[3]According to (7), $\Phi_{i,j}$ assigns a value 0 to those pixel locations which are corrupted by impulse noise and the value 1 to those pixel locations which are corrupted by Gaussian noise.

C. Componentwise Minimization

The resulting criterion function of (8) is still nonconvex and difficult to solve. Therefore, in this section, we propose an alternating minimization approach that decouples the energy functional into two parts; one for the estimation of u and the other for the estimation of the binary matrix Φ. For solving the problem under fixed Φ, the resultant optimization problem is convex if the penalty term $J(u)$ is convex. Similarly, under fixed u, Φ can be estimated in a single step.

1) *Estimation of u:* Under fixed Φ, the fidelity term over the set Ω_g is convex and quadratic, and the penalty term is convex (usually a nonsmooth term). The criterion function to estimate u is given by

$$\hat{u} = \arg\min_u \frac{1}{2}\|f - u\|_2^2 + \lambda_1 J(u) \quad (9)$$

2) *Estimation of Φ:* Under fixed u, $\mathcal{L}(u, \Phi)$ is a function of Φ only

$$\hat{\Phi} = \arg\min_{\Phi \in \{0,1\}^{mn \times p}} \frac{1}{2}\Phi\|f - u\|_2^2 - \lambda_2\Phi. \quad (10)$$

Since (10) is separable, it can be solved in a constant time as

$$\Phi = \begin{cases} 0; \text{ if } (f - u)_{i,j}^2/2 < \lambda_2 \\ 1; \text{ if } (f - u)_{i,j}^2/2 < \lambda_2 \\ 0 \text{ or } 1; \text{ if } (f - u)_{i,j}^2/2 = \lambda_2. \end{cases} \quad (11)$$

According to (9) and (10), λ_1 and λ_2 are the two hyperparameters set according to the noise level of g and v, respectively. For the initial estimation of Φ, rank-ordered absolute difference (ROAD) filter [32] is used. This is updated in every iteration as

it is especially important under RVIN where several iterations are needed to accurately detect the corrupted pixels under mixed Gaussian-impulse noise. A block diagram of the componentwise minimization *(CompoHyDen)* is depicted in Fig. 2. The noise simulation in the forward observation model is preceded by masking the image using the binary matrix Φ and $(\mathbb{I} - \Phi)$. This is made possible by the Hadamard product $(\odot)$ computation. The pixels decoupled using Φ and $\mathbb{I} - \Phi$ are then chosen for Gaussian (g) and impulse (v) noise simulation. During the inverse estimation, $\hat{u}$ and $\hat{\Phi}$ are found iteratively from the noisy image f using (9) and (10), respectively. This is also depicted in Fig. 2.

The choice of the penalty term $J(u)$ for Gaussian noise is deferred until Section IV-E. It will be a convex term that can be directly fed into (9).

D. Convergence Analysis and the Modified Objective Function

In this section, we show that (9) and (10) for the estimation of u and Φ yields a coordinatewise minimizer of $\mathcal{L}(u, \Phi)$ in a finite number of steps. In other words, we can state that a point $(\hat{u}, \hat{\Phi})$ is a coordinatewise minimizer of $\mathcal{L}(u, \hat{\Phi})$ and $\hat{\Phi}$ is a coordinatewise minimizer of $E^p(u)$ in (5).

Theorem 1: If we consider that $\tilde{u}$ is a local minimizer for $E^p(u)$ and $\Phi \in [0, 1]^{mn \times p}$ minimizes $\mathcal{L}(\tilde{u}, \Phi)$, then $(\tilde{u}, \tilde{\Phi})$ is the local minima for $\mathcal{L}(u, \Phi)$.

Proof: Assuming that $\tilde{u}$ is the local minimizer for $E^p(u)$, we can use a very small constant $\epsilon > 0$ such that whenever $\|u - \tilde{u}\| < \epsilon$, then $E^p(u) \geq E^p(\tilde{u})$. As a result, $\forall (u, \Phi)$ satisfying the condition $\|(u, \Phi) - (\tilde{u}, \tilde{\Phi})\| < \epsilon$, we also have $\|u - \tilde{u}\| < \epsilon$

$$\mathcal{L}(u, \Phi) \geq E^p(u) \geq E^p(\tilde{u}) = \mathcal{L}(\tilde{u}, \tilde{\Phi}). \tag{12}$$

Thus, we can conclude that $(\tilde{u}, \tilde{\Phi})$ is a local minimizer for $\mathcal{L}(u, \Phi)$. ∎

Theorem 2: If $\tilde{\Phi}$ is the coordinatewise minimum point for $\mathcal{L}(\tilde{u}, \Phi)$, then $(\tilde{u}, \tilde{\Phi})$ is a local minima for $\mathcal{L}(u, \Phi)$. Also, $\tilde{u}$ is a local minima of $E^p(u)$.

Proof: Since $\tilde{\Phi}$ provides a local minima for $\mathcal{L}(\tilde{u}, \Phi)$ and $\tilde{u}$ minimizes $\mathcal{L}(u, \tilde{\Phi})$, we have $\tilde{u}$ as the local minima of $E^p(u)$. Then, $(\tilde{u}, \tilde{\Phi})$ is the local minima of $\mathcal{L}(u, \Phi)$ from Theorem 1.

However, while solving the subproblem Φ^k for iteration k in (10), there can be many points of minima for $\mathcal{L}(u^k, \Phi)$. We are required to choose the best Φ to minimize $\mathcal{L}(u, \Phi)$, so that the algorithm converges to the local minima point of $E^p(u)$. ∎

Since there can be many potential candidates for Φ which minimizes $\mathcal{L}(u, \Phi)$, we resort to the following strategy. The objective function of (8) can be modified by appending a term $\tau\Phi r$ where r has the same dimension as Φ and u and τ is a small constant. Each entry $r_{i,j}$ in r is a random value uniformly sampled in the range [0,1]. Equation (8) is modified as

$$\acute{\mathcal{L}}(u, \Phi) = \arg\min_{u, \Phi \in [0,1]} \mathcal{L}(u, \Phi) + \tau\Phi r. \tag{13}$$

This ensures that the algorithm stops at local minima with probability 1. On the other hand, under (11), the subproblem

for estimating Φ is modified to

$$\Phi = \begin{cases} 0; \text{ if } (f - u)_{i,j}^2/2 + \tau r < \lambda_2 \\ 1; \text{ if } (f - u)_{i,j}^2/2 + \tau r < \lambda_2 \\ 0 \text{ or } 1; \text{ if } (f - u)_{i,j}^2/2 + \tau r = \lambda_2. \end{cases} \tag{14}$$

E. Vectorial NLTV as Regularization Term

A classical image restoration framework using Rudin-Other-Fatemi (ROF) [33] model of TV-based regularization estimates the local derivatives with respect to the adjacent pixels. This is called local TV. It is based on the assumption that individual pixels are surrounded by smooth regions punctuated by sharp discontinuities. This contributes to the piecewise approximation of images, which helps in noise removal and detail preservation. However, the local version of TV cannot distinguish fine structural details and textures from noise.

In order to overcome these limitations of a classical TV model, the interactions of pixels with its neighbors need to be explored. Here, the neighborhood is based not only on the spatial closeness but also closeness in terms of its intensity with other pixels over the entire spatial and spectral extent of the image. NLM is a classical approach by Buades et al. [34] to restore a pixel $x \in u$ by averaging the intensity levels over all the pixels based on neighborhood similarity decaying as a function of h

$$\omega_{u_0} = \frac{\exp(-d_\rho(u_0(x) - u_0(y))}{h^2} \tag{15}$$

where the distance d is computed by $d_\rho(u_0(x) - u_0(y)) = \int_\Omega G_\rho(t)|u(x + t) - u(y + t)|^2 \, dt$. G_ρ is a Gaussian kernel and h is the filtering parameter that controls the decay of ω as the function of Euclidean distance between image patches. The weight function ω satisfies the following properties:

1) $0 < \omega_{u_0} \leq 1$;
2) $\int_{\omega_{u_0}}(x, y) = 1$.

Since TV is ℓ_1-norm over image gradients, incorporating an NLTV prior on the image u yields $\nabla_\omega u(x, y) = (u(y) - u(x) \cdot \sqrt{\omega(x, y)} \forall y \in \omega$ for $\omega : \Omega \times \Omega \to \mathbb{R}$ and $u : \Omega \to \mathbb{R}$, as shown by Gilboa and Osher in [35]. A classical approach to image restoration composed of a data fidelity and NLTV term computes the similarity weights along the spectral dimension collectively. The objective function used to realize this is given below

$$\hat{u} = \arg\min_u \frac{1}{2}\|f - u\|_2^2 + \lambda \nabla_{\omega_0}\|u\|_1. \tag{16}$$

However, the above equation uses NLTV along each band separately [36], [37]. This misses the similarity among pixels along the spectral axis.

Discretization of the nonlocal gradient ∇_ω on $u \in \mathbb{R}^{mn \times p}$ involves a linear operator K [38]. Computation of K over u yields a 3-D matrix Ku whose first, second, and third dimensions correspond to the pixels, weighted differences of the pixels and the number of bands. For $Ku \in \mathbb{R}^{m \times n \times p}$, each

$(Ku)_{:,:,p}$ is given by (17),

$$
\begin{bmatrix}
0 & \omega_{1,2}(u_{1,p}-u_{2,p}) & \dots & \omega_{1,p}(u_{1,p}-u_{m,p}) \\
\omega_{2,1}(u_{2,p}-u_{1,p}) & 0 & \dots & \omega_{2,p}(u_{2,p}-u_{m,p}) \\
\vdots & \vdots & \ddots & \vdots \\
\omega_{n,1}(u_{n,p}-u_{1,p}) & \omega_{n,3}(u_{n,p}-u_{3,p}) & \dots & 0
\end{bmatrix}
\tag{17}
$$

where the first subscript in each entry denotes the linear indexing of pixels for each layer (the Casorati representation of 3-D data, as mentioned in Section III) and the second dimension denotes the spectral dimension. Considering that $\nabla_\omega u$ is implemented using Ku, (16) is modified as

$$
\hat{u} = \arg\min_{u} \frac{1}{2}\|f-u\|_2^2 + \lambda\|Ku\|_{\infty,1,1}.
\tag{18}
$$

The general $\ell_{p,q,r}-$norm over a matrix X is given by

$$
\|X\|_{p,q,r} = \left(\sum_i \left(\sum_j \left(\sum_k |X_{i,j,k}|^p \right)^{q/p} \right)^{r/q} \right)^{1/r}
\tag{19}
$$

where r,q,p are taken along the first, second, and third dimensions, respectively, [39] [40] [41]. Typically, we consider $\ell_{\infty,1,1}$ because the interchannel coupling is more in $\ell_\infty-$norm than in ℓ_2 or ℓ_1 norm. Splitting the image gradient in horizontal (∇_h) and vertical (∇_v) components for $\ell_{\infty,1,1}-$norm yields the following expression:

$$
\int_\omega \left(\max_{\forall p}[\nabla_h u(x)] + \max_{\forall p}[\nabla_v u(x)] \right).
\tag{20}
$$

The nonlocal regularization interacts only among the pixels locally within the search window $K > 0$. In other words, $\omega(x,y) = 0$ for $\|x-y\|_\infty > K$. The similarity weight between the pixel x and y is defined by

$$
\omega(x,y) = \begin{cases}
\frac{1}{C(x)} e^{-\frac{1}{h^2}\sum_{t\in\mathcal{N}_0}\|u_0(x+t)^2-u_0(y+t)^2\|} \\
\quad ; \text{if } \|x-y\|_\infty \le K \\
0; \text{ otherwise}
\end{cases}
\tag{21}
$$

where $\mathcal{N}_0$ is the comparison window centered at 0 and h has the same usual meaning as defined in (15). C is the normalization factor defined by

$$
C(x) = e^{-\frac{1}{h^2}\sum_{\{y:\|x-y\|_\infty\le K\}}\|u_0(x+t)^2-u_0(y+t)^2\|}.
\tag{22}
$$

F. Final Algorithm

For the minimization of objective function of (18), we make use of primal-dual hybrid gradient (PDHG) of the form [42]

$$
\hat{u} = \arg\min_{u} \sum_{i=1}^{N} l_i(T_i u)
\tag{23}
$$

where l_i is a term in the objective function and T_i is an operator, both indexed by i. N is the total number of terms in the objective function. A generalized proximal projection of a term l_i in the

---

Algorithm 1: *CompoHyDen.*

Require: $u_0 \in \mathbb{R}^{mn\times p}$, $\tau > 0$, $\sigma > 0$, $\rho >$
$0, f, \lambda_1, \lambda_2, \epsilon,\ i = 1\cdots N,\ k = 1$
1: **Initialise:** $v_0 = 0$, $x_{0,i-1} = u_0$, Φ^0, $k = 1\dots K$
2: **while** $\mathcal{L}(u^k, \Phi^k) - \mathcal{L}(u^{k-1}, \Phi^{k-1}) > \epsilon$ **do**
3:   **for** $i \in 1\dots N$ **do**
4:     $q_{k,i} = x_{k,i} + \sigma \cdot T_i(2v_k - u_{k-1})$
5:     $p_{k,1} = q_{k,i} - \sigma \cdot \text{prox}_{l_i/\sigma}(q_{k,i}/\sigma)$
6:     $x_{k,i} = \rho \cdot p_{k,i} + (1-\rho)x_{k-1,i}$
7:   **end for**
8:   $v_k = u_{k-1} - \sum_{i=1}^{N} \tau T_i^* x_{k,i}$
9:   $u_k = \rho v_k + (1-\rho)u_{k-1}$
10:   Estimate Φ^k from (14)
11:   $k = k+1$
12: **end while**

---

objective function of (23) is given by [43]

$$
\text{prox}_\gamma l_i(y) = \arg\min_{u} \left\{ l_i(u) + \frac{1}{2\gamma}\|u-y\|_2^2 \right\}
\tag{24}
$$

with $\gamma > 0$ playing the role as the step-size parameter in any gradient-based optimization technique.

1) Considering that $y = T_1 u$ where $T_1 = I$

$$
\text{prox}_\gamma l_1(y) = \arg\min_{u} \frac{1}{2}\|f-u\|_2^2 + \frac{1}{2\gamma}\|u-y\|_2^2
\tag{25}
$$

$$
= \frac{y + \gamma f}{1 + \gamma}.
\tag{26}
$$

2) Similarly, considering that $y = T_2 u$ where $T_2 = K$

$$
\text{prox}_\gamma l_2(y) = \arg\min_{u} \left\{ \|Ku\|_{\infty,1,1} + \frac{1}{2\gamma}\|u-y\|_2^2 \right\}.
\tag{27a}
$$

Because the outer norms in (18) are in ℓ_1 form, the problem of estimating $\ell_{\infty,1,1}$ decouples along the first and second dimensions and the problem is reduced to the estimation of proximal operator of $\ell_\infty-$norm at each component [44]. This is equivalent to the projection onto L_1-ball (see Appendix A), given by

$$
= y - \text{Proj}_{\|\cdot\|_1\le 1}\left(\frac{y}{\lambda}\right).
\tag{27b}
$$

The final algorithm for solving (8) is given by the following. where ϵ is used as the stopping criteria, the initial value of the matrix Φ^0 is obtained from the ROAD filter [32] which is used for the detection of impulse corrupted pixels under RVIN. K is the number of iterations indexed by the subscript k and N is the number of terms in the objective function of (16) (here, $N = 2$). λ_1 and λ_2 are the hyperparameters given in (8). Initial estimates are given by u_0 and v_0. τ and σ are the proximal operators while ρ is the relaxation parameter.

V. EXPERIMENTAL RESULTS AND DISCUSSION

In this section, we conduct extensive experiments on synthetically corrupted hyperspectral data and those obtained from real hyperspectral sensors.

A. Experimental Setup

For experimentation purposes, all the images are normalized in the range [0,1] prior to noise simulation. Cases 1 and 3 are the homogeneous noise settings, while other cases are heterogeneous in nature. This distinction is made on the basis of the level and types of noise used to corrupt different bands of the 3-D data. Under homogeneous settings, the same level of noise is used to corrupt each band. On the other hand, different noise levels can be present in different bands in heterogeneous settings. Anisotropic noise in heterogeneous settings is difficult to handle as compared to the same noise levels added to all the bands. A comprehensive description of the noise settings is discussed below.

1) *Case 1:* For mean zero and standard deviation σ, denoted by $\mathcal{N} \sim (0, \sigma)$, three different levels of Gaussian noise are simulated that are identically distributed across all the layers with $\sigma = 0.02, 0.06, 0.1$.

2) *Case 2:* Here, Gaussian noise is nonidentically distributed (non-iid) with a signal-to-noise ratio (SNR) having a range of SNR $\sim$ U(10, 30) (uniformly sampled between 10 and 30).

3) *Case 3:* Identical to case 1 but here, RVIN denoted by $p\%$ is considered along with different values for σ such that $(\sigma, p) = (0.04, 6\%), (0.06, 10\%), (0.08, 15\%)$.

4) *Case 4:* Parameters are identical to case 2. However, along with noniid Gaussian noise, a noniid RVIN denoted by $p\%$ is used such that SNR $\sim$ U(20, 30) and p $\sim$ U(5%, 20%).

5) *Case 5:* Similar to case 2 with a different range of SNR $\sim$ U(10, 20) and 40% stripe noise. The stripe noise here is simulated by taking into consideration the method proposed in [45] and [46]. When we say that there is $x\%$ stripe noise, we indicate that x percent of all the layers in the given datacube is randomly selected as a viable candidate for stripe noise addition. From the chosen candidate layer, $20 - 40$ number of columns are randomly selected. The intensities of the pixels in these columns are either increased or decreased in accordance with the mean of the pixel intensities of the chosen layer.

6) *Case 6:* Identical to case 5 with the exception that the range for the number of columns is $5-15$. Also, instead of stripe noise, deadlines are added to 50% of the layers.

7) *Case 7:* Similar to case 5 in terms of the range of stripe noise (40%) but with SNR $\sim$ U(20, 30) and p $\sim$ U(5%, 20%).

8) *Case 8:* Similar to instance 7, except that deadlines (50%) are introduced; in place of stripe noise.

9) *Case 9:* Pairing of simulation from cases 7 and 8. Here, stripe noise, deadlines, as well as Gaussian and impulse noise, are introduced into the data.

Under the above noise settings for synthetic and real data, some state-of-the-art methods are used for visual and quantitative comparisons. These methods include: TV-regularized low-rank matrix factorization for hyperspectral image restoration (LRTV) [47], hyperspectral image restoration via TV regularized low-rank tensor decomposition (LRTDTV) [48], denoising hyperspectral image with noniid noise structure (NMoG) [22], double-factor-regularized low-rank tensor factorization for mixed noise removal in hyperspectral image (LRTFDFR) [49], hyperspectral image denoising using factor group sparsity-regularized nonconvex low-rank approximation (FGSLR) [50], hyperspectral image denoising based on global and nonlocal low-rank factorizations (GLF) [51], mixed noise removal in hyperspectral image via low-fibered-rank regularization (3-DlogTNN) [52], hyperspectral image restoration via local low-rank matrix recovery and Moreau-enhanced TV (EnhancedTV) [53] and hyperspectral mixed noise removal by ℓ_1-norm-based subspace representation (L1HyMixDe) [54].

To support the visual results, we have used five separate full reference image quality assessment metrics, including two spectral-specific indicators, to compare the relative performance of different methods. On the one hand, spatial metrics include peak PSNR, structural similarity index (SSIM) [55], and feature similarity index (FSIM) [56], while mean spectral angle mapper (MSAM) [57] and Erreur Relative Globale Adimensionnelle de Synthèse (ERGAS) [58] are the spectral metrics. Better performance of a restoration method is judged by higher values of the spatial metrics and lower values of the spectral metrics. While drawing comparisons, an average of these metrics over all bands of the image is considered.

B. Experiments on Synthetic Data

The synthetic data used in this work have been derived from the *Cuprite*[4] dataset and the *Interdisciplinary Computer Vision Laboratory (ICVL)*[5] dataset. The airborne visible/infrared imaging spectrometer (AVIRIS) sensor recorded the *Cuprite* dataset, with 224 spectral bands in the wavelengths range of 370–2480 nm. The initial spatial dimension was 512×614. But a cropped region of 256×256 pixels was used for the experimentation purposes. Images in the ICVL dataset were captured using the *Specim PS Kappa DX4* hyperspectral camera. While this work was being written, more than 200 photos were already part of the ICVL dataset, including photos from urban, suburban, indoor, and plant lifelike acquisition settings. Each image has a size of $1392 \times 1300 \times 519$ and has a wavelength ranging from 400 to 1000 nm with 1.25 nm increments. However, for all practical purposes, we used 31 band images which are also part of the same existing dataset. To reduce the computational burden while processing using comparing methods, the spatial dimension was down-sampled to 512×512 pixels. Each layer in both the datasets was noise simulated under cases 1–9 (mentioned previously).

Fig. 3 helps visualize the denoising results of the simulated *Cuprite* dataset under noise case 1. Images are shown in their

---

[4]Obtained from: https://aviris.jpl.nasa.gov/data/free_data.html
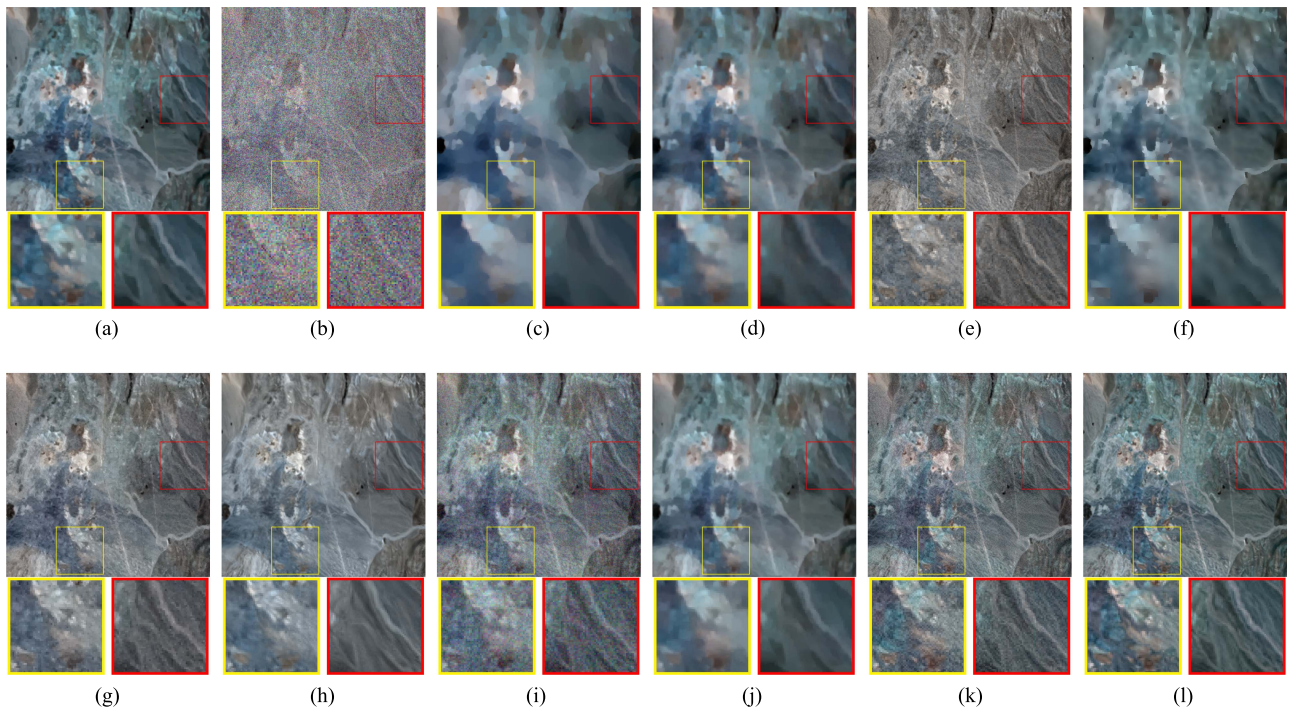[5]Obtained from:https://icvl.cs.bgu.ac.il/hyperspectral/

Fig. 3. Denoising results of simulated Cuprite dataset under noisy case 1: ($\sigma = 0.02$). Images are displayed in their pseudocolor representation by combining three channels (red: 50, green: 80, blue: 90). (a) Groundtruth. (b) Noisy. (c) LRTV. (d) LRTDTV. (e) NMoG. (f) LRTFDFR. (g) FGSLR. (h) GLF. (i) 3-DlogTNN. (j) EnhancedTV. (k) L1HyMixDe. (l) *CompoHyDen*.

pseudocolor representation by concatenating three grayscale bands (red: 50, green: 80, blue: 90). In Fig. 3, denoising results on an image corrupted by iid Gaussian noise with standard deviation $\sigma = 0.02$ are shown with visual comparison with nine other competing methods. From the zoomed-in portion of each image, the proposed model evidently denoises the images better. Also, the results are sharp and more detailed, with considerably less blur. Visual result of the proposed methodology depicted in the figure shows a significant contrast preserving behavior compared to other methods. Visual results generated by methods like NMoG and GLF fail to remove the grainy texture, stripes, and other artifacts from the image, while LRTDTV loses details in an attempt to recover the corrupted observation. The proposed method reduces these anomalies brought about by the noise and postprocessing artifacts.

Similarly, on the ICVL dataset, Fig. 4 gives the visual results under noise case 3 with the images being displayed in their pseudocolor representation by combining three bands (red: 30, green: 20, blue: 10). For Fig. 4, the iid Gaussian noise with $\sigma = 0.04$ and RVIN with $p = 6\%$ corrupts the image. The visual comparison shows that the proposed method does effective denoising without introducing unnecessary blur during noise removal. At the same time, it maintains the contrast present in the ground truth data.

To aid visual analysis, image restoration performance must be quantified. This is achieved by employing metrics such as PSNR, SSIM, MSAM, EGRAS, and FSIM. Because PSNR and SSIM are best suited for 2-D data, the graphs in Fig. 5 (for PSNR) and Fig. 6 (for SSIM) show these metrics plotted against

a spectrum of band numbers ranging from 1 to 224, for the Cuprite dataset. Higher values for both these metrics indicate good reconstruction quality when compared to the groundtruth signal. Whereas PSNR provides pixel-level similarity, SSIM quantifies perceptually appealing visual results that correlate with the human visual system (HVS). The two figures point to high PSNR (see Fig. 5) and SSIM (see Fig. 6) values for the proposed method for five distinct noise cases (1, 3, 5, 7, and 9) across layers, outperforming the state-of-the-art methods in most cases. However, due to the inherently low input SNR in some bands, there are some occasional drops around layers 130 and 160. According to the graphs, the second, third, and fourth best-performing methods for all cases are FGSLR, GLF, and L1HyMixDe. An aggregate analysis of the restoration performance is necessary to estimate the overall accuracy of different methods. Therefore, in Table I, we have tabulated the results of all the metrics for *Cuprite* dataset.

Fig. 7 gives an in-depth insight into the spectral signature for the *Cuprite* dataset in various cases and pixel locations, which help in drawing a comparison of reconstruction accuracy between the ground truth, proposed methodology *(CompoHy-Den)*, and other approaches. Its main aim is to compare the proposed denoising model's reconstruction accuracy to those of the other techniques mentioned in the work. For the ground-truth plot, the areas shown with arrows and lines indicate the layers that have a distinct change in spectral signature from the results obtained using various methods. The pixel locations are selected at random and for each plotted case, a great degree of similarity with the ground truth validates the efficiency of the proposed
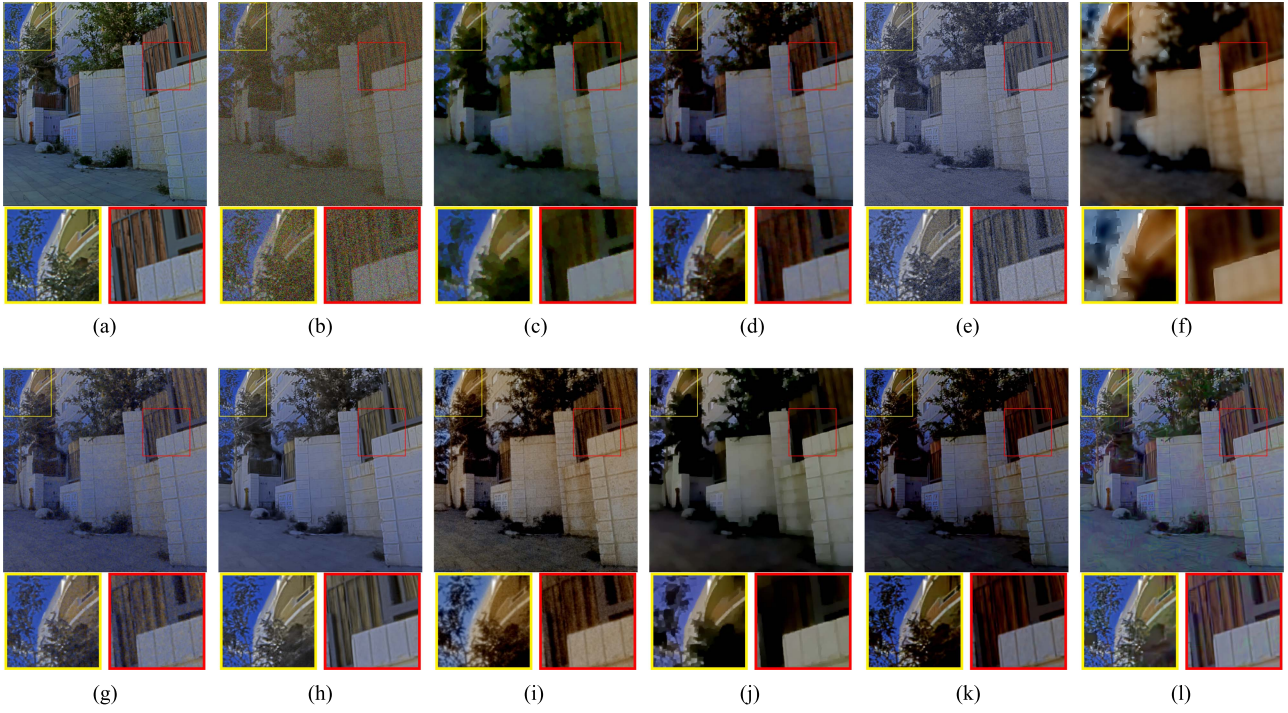
Fig. 4. Denoising results of simulated ICVL dataset under noisy case 3: ($\sigma = 0.04$, $p = 6\%$). Images are displayed in their pseudocolor representation by combining three channels (red: 30, green: 20, blue: 10). (a) Groundtruth. (b) Noisy. (c) LRTV. (d) LRTDTV. (e) NMoG. (f) LRTFDFR. (g) FGSLR. (h) GLF. (i) 3-DlogTNN. (j) EnhancedTV. (k) L1HyMixDe. (l) *CompoHyDen*.

Fig. 5. Layerwise evaluation of PSNR for the Cuprite dataset for (a) case 1, (b) case 3, (c) case 5, (d) case 7, and (e) case 9. The line shown in black represents the results obtained by our proposed methodology (*CompoHyDen*). PSNR achieves the best values for all the cases with exceptional drop around more noisy layers.

Fig. 6. Layerwise evaluation of SSIM for the Cuprite dataset for (a) case 1, (b) case 3, (c) case 5, (d) case 7, and (e) case 9. The line shown in black represents the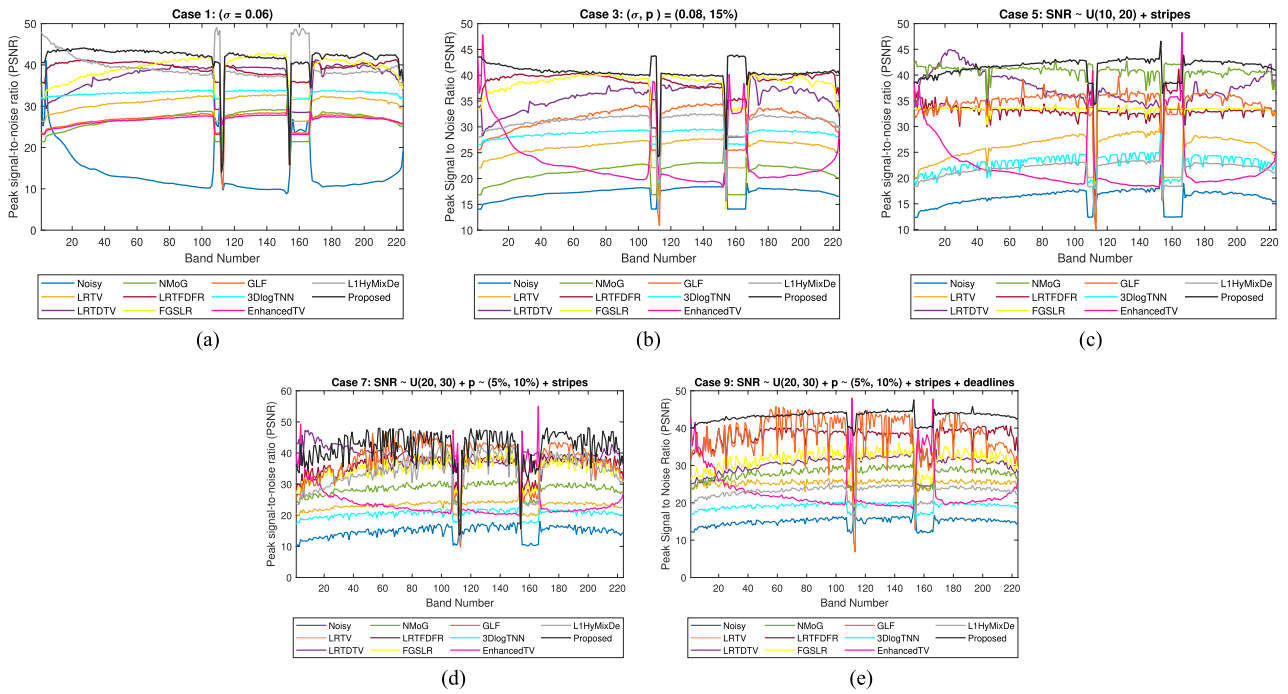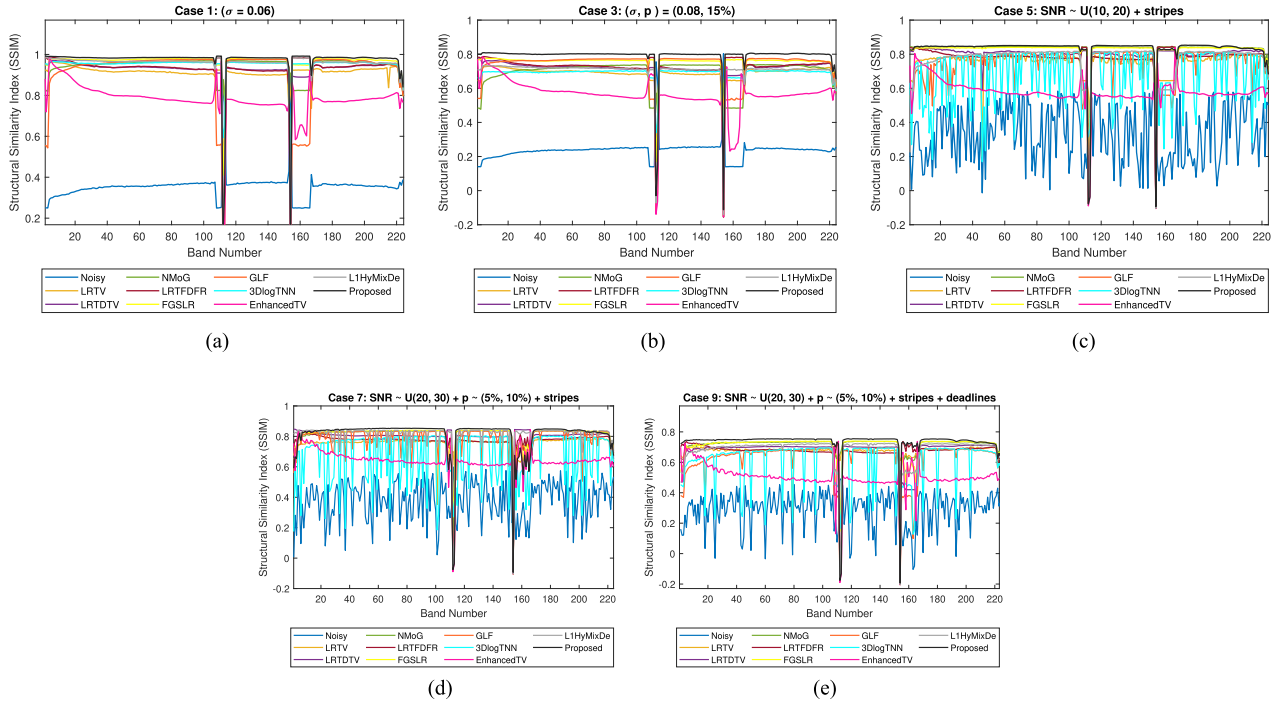 results obtained by our proposed methodology (*CompoHyDen*). SSIM achieves the best values for all the cases with exceptional drop around more noisy layers.
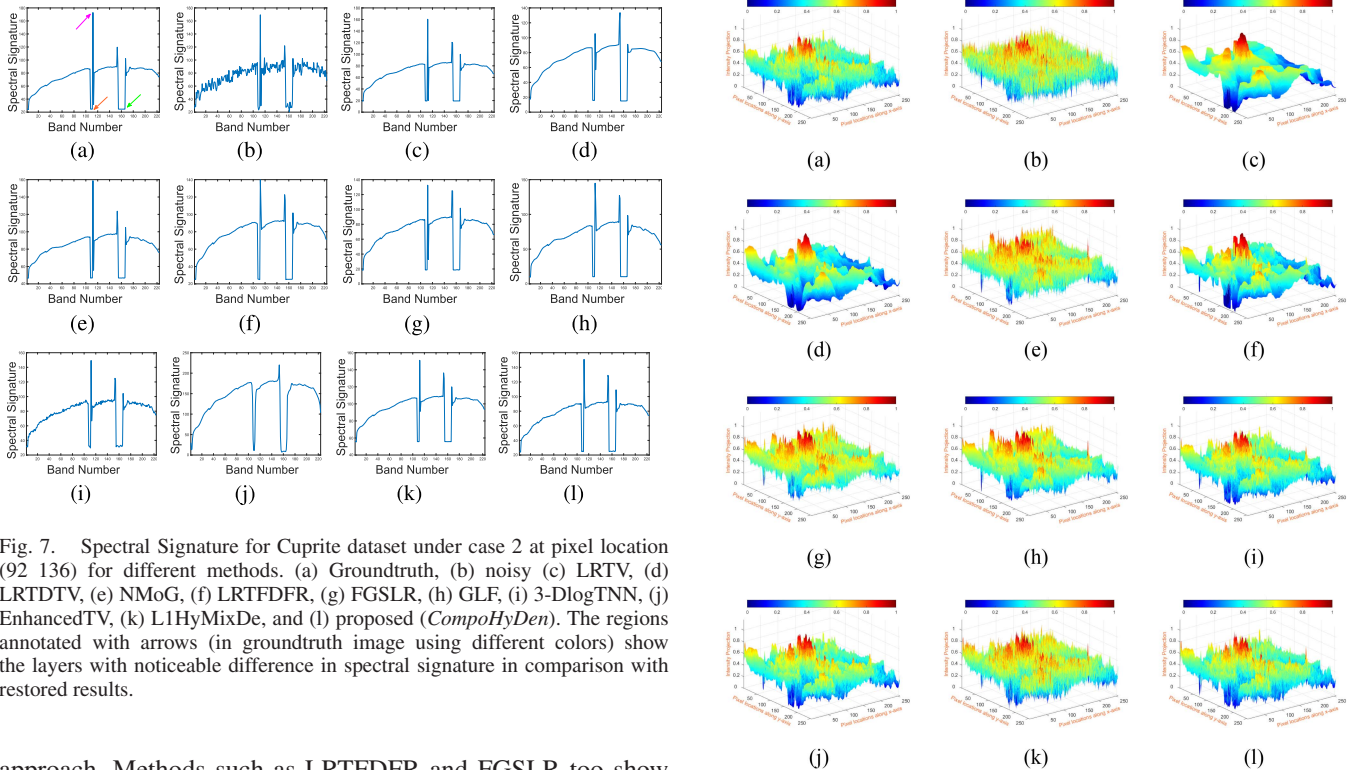
Fig. 7. Spectral Signature for Cuprite dataset under case 2 at pixel location (92 136) for different methods. (a) Groundtruth, (b) noisy (c) LRTV, (d) LRTDTV, (e) NMoG, (f) LRTFDFR, (g) FGSLR, (h) GLF, (i) 3-DlogTNN, (j) EnhancedTV, (k) L1HyMixDe, and (l) proposed (*CompoHyDen*). The regions annotated with arrows (in groundtruth image using different colors) show the layers with noticeable difference in spectral signature in comparison with restored results.

approach. Methods such as LRTFDFR and FGSLR too show promising results under cases 4 and 5. The 3-D graphs in Fig. 8 give the intensity projection for a particular layer. Here, the intensity levels are plotted along the *z*-axis for the corresponding pixel locations through the horizontal and vertical extent of

Fig. 8. Intensity projection for layer 50 under case 1: ($\sigma = 0.06$) using different methods for Cuprite dataset. (a) Groundtruth, (b) noisy, (c) LRTV, (d) LRTDTV, (e) NMoG, (f) LRTFDFR, (g) FGSLR, (h) GLF, (i) 3-DlogTNN, (j) EnhancedTV, (k) L1HyMixDe, and (l) proposed (*CompoHyDen*).

TABLE I
QUANTITATIVE EVALUATION USING MPSNR, MSSIM, MSAM, ERGAS, AND MFSIM METRICS FOR CUPRITE DATASET

	Noise Level	Metrics	Noisy	LRTV	LRTDTV	NMoG	LRTFDFR	FGSLR	GLF	3DlogTNN	EnhancedTV	L1HyMixDe	CompoHyDen
Case 1	$\sigma = 0.02$	MPSNR	33.68	35.19	42.23	**45.84**	37.98	31.67	29.47	39.33	12.64	20.82	40.76
		MSSIM	0.762	0.959	0.961	**0.986**	0.935	0.962	0.929	0.979	0.726	0.921	0.927
		MSAM	4.02	**1.86**	4.1	2.24	3.34	4.37	7.61	2.65	9.89	7.10	3.32
		ERGAS	4.448	0.236	0.227	**0.128**	0.223	0.424	0.603	0.182	3.308	1.264	0.19
		MFSIM	0.89	0.968	0.995	0.995	0.936	0.993	0.99	0.993	0.989	**0.996**	0.946
	$\sigma = 0.06$	MPSNR	21.54	30.75	38.71	26.69	38.98	38.79	26.71	33.01	13.86	**41.97**	34.64
		MSSIM	0.355	0.915	0.922	0.945	0.932	**0.964**	0.915	0.95	0.781	0.953	0.915
		MSAM	9.77	3.65	6.4	5.49	3.68	3.28	7.49	**3.21**	9.47	3.94	3.43
		ERGAS	19.18	0.44	0.384	0.737	0.22	0.233	0.696	0.316	2.845	**0.207**	0.274
		MFSIM	#VALUE!	0.925	0.986	0.988	0.932	0.989	0.987	0.987	0.957	**0.99**	0.922
	$\sigma = 0.01$	MPSNR	17.49	26.91	35.93	20.62	37.41	**41.1**	29.7	25.36	13.27	20.69	35.29
		MSSIM	0.218	0.892	0.889	0.889	0.927	**0.954**	0.914	0.774	0.757	0.855	0.907
		MSAM	12.63	5.03	8.04	8.38	3.51	**3.07**	7.36	5.64	9.35	7.29	3.88
		ERGAS	30.521	0.678	0.544	1.411	0.231	**0.182**	0.594	0.763	3.055	1.285	0.281
		MFSIM	0.574	0.899	0.981	0.981	0.92	**0.986**	0.981	0.956	0.931	0.978	0.911
Case 2	SNR∼ U(10, 30)	MPSNR	19.58	24.31	**44.13**	19.9	39.29	36.76	29.86	38.86	12.26	22.87	38.26
		MSSIM	0.686	0.914	**0.977**	0.896	0.931	0.975	0.966	0.975	0.718	0.937	0.923
		MSAM	9.66	5.19	2.97	9.59	3.65	3.50	5.96	**2.68**	10.5	6.48	3.47
		ERGAS	25.319	0.867	**0.156**	1.548	0.218	0.277	0.475	0.186	3.407	1.013	0.216
		MFSIM	0.857	0.959	**0.998**	0.993	0.929	0.994	0.99	0.992	0.981	0.997	0.939
Case 3	$\sigma = 0.04, p = 6\%$	MPSNR	23.87	37.1	40.56	27.64	38.28	31.33	29.4	38.20	12.97	20.44	40.09
		MSSIM	0.455	0.937	0.943	0.958	0.927	0.953	0.931	**0.971**	0.748	0.913	0.919
		MSAM	7.88	**1.87**	5.26	4.18	3.95	4.38	7.3	2.89	9.87	6.51	3.39
		ERGAS	14.283	**0.188**	0.293	0.612	0.251	0.429	0.585	0.202	3.16	1.274	0.199
		MFSIM	0.734	0.939	0.989	0.99	0.925	0.991	0.988	0.991	0.975	**0.993**	0.927
	$\sigma = 0.06, p = 10\%$	MPSNR	21.1	25.84	36.64	23.49	32.17	39.15	27.88	23.51	13.99	**39.66**	38.34
		MSSIM	0.317	0.9	0.9	0.926	0.923	**0.961**	0.926	0.915	0.783	0.949	0.914
		MSAM	10.38	4.39	7.33	6.51	3.60	**3.26**	7.04	4.92	9.33	4.23	3.55
		ERGAS	20.124	0.713	0.492	1.014	0.34	0.224	0.622	0.891	2.799	0.236	**0.216**
		MFSIM	0.647	0.92	0.985	0.987	0.922	0.988	0.986	0.986	0.953	**0.989**	0.917
	$\sigma = 0.08, p = 15\%$	MPSNR	17.2	25.93	37.34	21.18	38.58	**41.1**	31.29	28.54	13.46	30.98	35.54
		MSSIM	0.238	0.89	0.901	0.898	0.924	**0.954**	0.934	0.888	0.763	0.904	0.91
		MSAM	12.09	5.11	7.68	7.86	3.78	**3.07**	6.64	4.20	9.47	4.71	3.5
		ERGAS	31.315	0.742	0.469	1.314	0.227	**0.182**	0.501	0.515	2.986	0.43	0.26
		MFSIM	0.593	0.905	0.982	0.983	0.915	**0.986**	0.982	0.976	0.94	0.983	0.909
Case 4	SNR∼U(20, 30), p∼U(5%, 20%)	MPSNR	26.86	35.78	36.43	32.04	35.9	34.23	33.9	**38.93**	13.84	37.62	36.88
		MSSIM	0.531	0.933	0.913	0.964	0.913	0.956	0.956	0.968	0.791	**0.969**	0.915
		MSAM	7.81	**3.02**	7.51	4.92	4.74	4.57	6.7	3.66	8.51	4.51	4.07
		ERGAS	11.393	0.287	0.438	0.495	0.322	0.38	0.437	0.256	2.87	0.303	**0.251**
		MFSIM	0.773	0.938	0.988	**0.994**	0.902	0.991	0.989	0.991	0.972	0.993	0.924
Case 5	SNR∼ U(10, 20) + stripes	MPSNR	16.24	26.03	24.47	**40.51**	33.1	33.19	34.72	22.84	12.49	21.75	34.62
		MSSIM	0.628	0.905	0.722	**0.979**	0.93	0.976	0.971	0.826	0.73	0.922	0.919
		MSAM	11.22	6.51	10.18	5.12	3.62	**3.03**	5.97	7.48	10.02	7.55	3.63
		ERGAS	36.175	0.831	1.606	**0.258**	0.313	0.303	0.355	1.047	3.336	1.181	0.278
		MFSIM	0.827	0.957	0.996	**0.996**	0.934	0.994	0.99	0.965	0.985	0.995	0.942
Case 6	SNR∼ U(10, 20) + deadlines	MPSNR	22.48	**34.91**	20.09	30.06	33.56	32.8	29.15	20.24	11.88	19.73	32.31
		MSSIM	0.586	0.944	0.603	0.968	0.916	**0.978**	0.953	0.817	0.707	0.908	0.917
		MSAM	9.41	**2.64**	11.85	5.79	4.99	2.79	6.55	8.13	10.55	7.52	3.81
		ERGAS	16.938	**0.27**	2.661	0.491	0.391	0.308	0.532	1.301	3.597	1.428	0.339
		MFSIM	0.767	0.955	0.991	**0.996**	0.923	0.994	0.988	0.958	0.979	**0.996**	0.942
Case 7	SNR∼ U(20, 30), p∼ U(5%, 20%) + stripes	MPSNR	22.72	23.10	21.4	28.31	35.68	34.72	37.74	20.47	14.52	**41.97**	38.67
		MSSIM	0.678	0.902	0.642	0.962	0.919	**0.965**	0.952	0.811	0.791	0.963	0.921
		MSAM	8.27	5.55	10.58	5.34	4.50	4.08	6.94	8.06	9.33	4.75	**3.53**
		ERGAS	17.592	0.988	2.249	0.59	0.319	0.345	0.428	1.326	2.677	0.249	**0.213**
		MFSIM	0.837	0.954	0.992	**0.995**	0.915	0.989	0.967	0.982	0.991	0.937
Case 8	SNR∼ U(20, 30), p∼ U(5%, 20%) + deadlines	MPSNR	26.06	28.90	40.33	**44.67**	37.75	32.25	33.05	22.51	12.79	22.22	35.69
		MSSIM	0.654	0.938	0.948	**0.98**	0.924	0.96	0.947	0.872	0.753	0.932	0.919
		MSAM	7.52	**2.65**	5.33	3.74	4.10	4.38	7.20	7.30	9.64	6.16	3.62
		ERGAS	11.122	0.472	0.279	**0.193**	0.256	0.406	0.492	1.019	3.277	1.057	0.261
		MFSIM	0.82	0.954	0.993	**0.996**	0.915	0.993	0.989	0.97	0.977	0.995	0.937
Case 9	SNR∼ U(20, 30), p∼ U(5%, 20%) + stripes + deadlines	MPSNR	19.96	25.35	20.78	27.82	37.53	31.38	**41.05**	19.14	13.25	23.09	36.04
		MSSIM	0.688	0.925	0.626	0.965	0.922	0.957	**0.972**	0.856	0.752	0.934	0.921
		MSAM	7.85	3.60	12.19	4.51	4.16	4.54	6.00	7.67	9.87	6.66	**3.54**
		ERGAS	22.434	0.717	2.515	0.608	0.266	0.436	0.302	1.504	3.092	1.006	**0.252**
		MFSIM	0.863	0.956	0.992	**0.995**	0.912	0.993	0.99	0.983	0.983	**0.995**	0.938

The best values are highlighted in bold.

the 2-D image layer (along the *x*- and *y*-axes). It helps in understanding how various methods perform at a pixel level when contrasted with the ground truth. Other than the promising plots of the proposed methodology, results vary from poor for LRTV and LRTDTV to considerably good for EnhancedTV and L1HyMixDe.

C. Experiments on Real Data

For experiments involving real-world data, we use the *Urban* dataset[6] obtained from hyperspectral digital imaging collection experiment (HYDICE) sensor covering a ground area of 2 m ×2 m. The resultant hyperspectral dataset is acquired in the wavelength range 440–2500 nm having 210 spectral bands. The spatial dimension is 307×307 pixels. Fig. 9 shows the

[6]Obtained from: https://rslab.ut.ac.ir/data

denoising results on the urban dataset for layer 200 using various denoising techniques. From the zoomed-in portions, it it is evident that the proposed methodology reconstructs the image better and is less pixelated. Also, our method does not blur the recovered image like LRTV and LRTDTV. This is further supported by the contrast preserving property of the proposed methodology *(CompoHyDen)*.

Any natural image is composed of mostly smooth sections punctuated by sharp change in contrast or edges. These are the regions of high-frequency components. However, noise also contributes to high-frequency. This effect can be quantized by plotting the horizontal and vertical mean profiles of the noisy and restored images. Mean profiles of noisy images have random spikes, which are less prominent in denoised versions of the same image. Fig. 10 plots the horizontal mean profile for layer 205 of the Urban dataset. In the horizontal mean profile, the
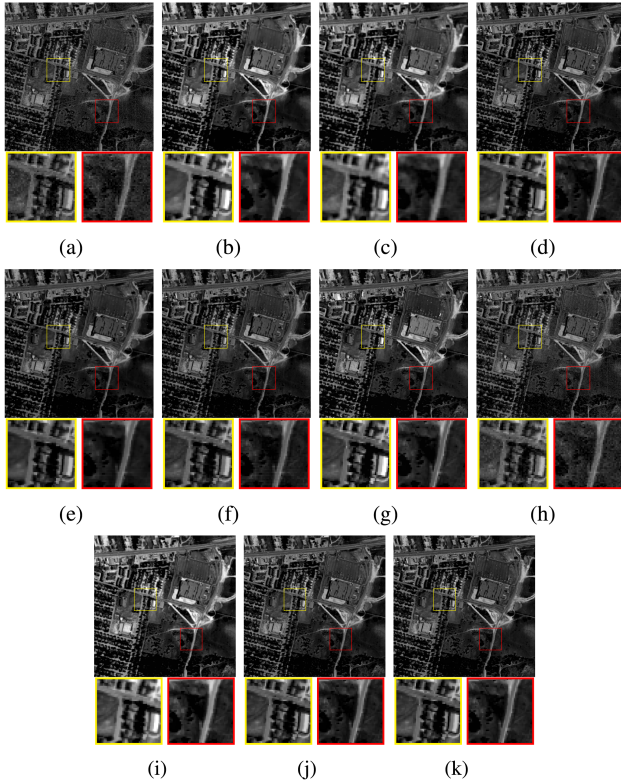
Fig. 9. Denoising results of urban dataset for layer 200. (a) Noisy, (b) LRTV, (c) LRTDTV, (d) NMoG, (e) LRTFDFR, (f) FGSLR, (g) GLF, (h) 3DlogTNN, (i) EnhancedTV, (j) L1HyMixDe, and (k) proposed (*CompoHyDen*).
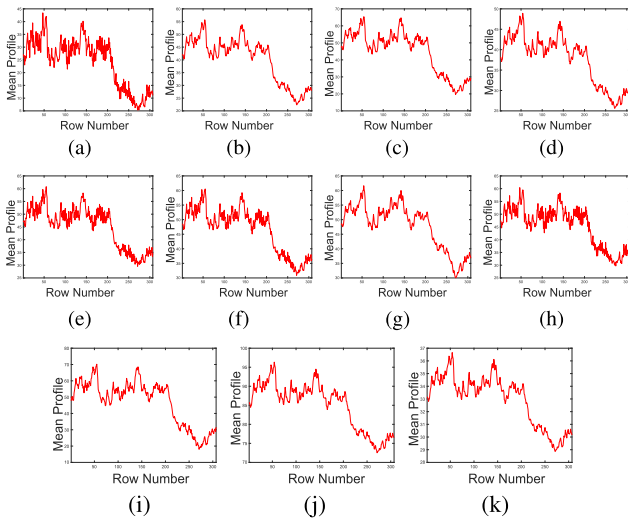

Fig. 10. Horizontal mean profile for the layer 205 for Urban dataset. (a) Noisy, (b) LRTV, (c) LRTDTV, (d) NMoG, (e) LRTFDFR, (f) FGSLR, (g) GLF, (h) 3-DlogTNN, (i) EnhancedTV, (j) L1HyMixDe, and (k) proposed (*CompoHyDen*).

mean intensity levels are plotted against the number of rows in the considered image band. In the graphs of LRTFDFR and FGSLR, spikes are not smoothed out while L1HyMixDe and the proposed method generate smoother plots. Similarly, a plot between the column number and the corresponding mean intensity levels are obtained in the vertical mean profile (see
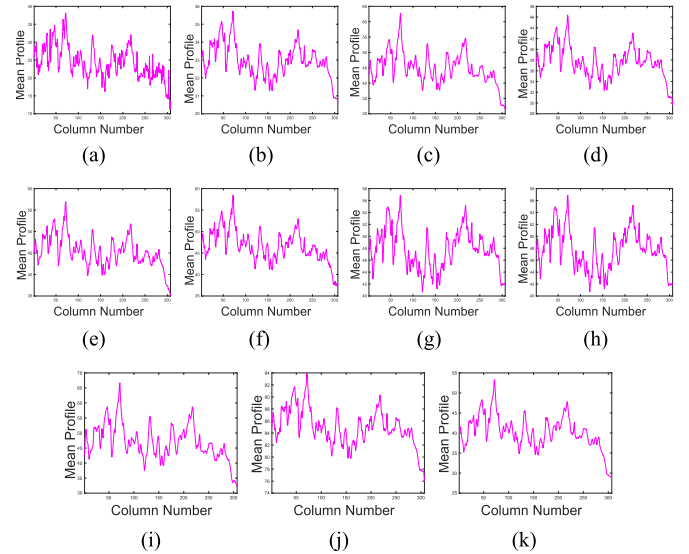

Fig. 11. Veritcal mean profile for the layer 205 for Urban dataset. (a) Noisy, (b) LRTV, (c) LRTDTV, (d) NMoG, (e) LRTFDFR, (f) FGSLR, (g) GLF, (h) 3-DlogTNN, (i) EnhancedTV, (j) L1HyMixDe, and (k) proposed (*Compo-HyDen*).

TABLE II
NO REFERENCE SPATIAL-SPATIAL IMAGE QUALITY ASSESSMENT [59] FOR
URBAN DATASET

LRTV	LRTDTV	NMoG	LRTFDFR	FGSLR
12.39	15.69	12.48	13.04	12.40
GLF	**3DlogTNN**	**EnhancedTV**	**L1HyMixDe**	***CompoHyDen***
12.46	12.39	12.85	12.12	**11.58**

Fig. 11). Here, EnhancedTV and the proposed algorithm show better results while mapping the mean vertical intensities but GLF and 3-DlogTNN are underperforming.

For images obtained from real hyperspectral sensors, reference/groundtruth data are barely available. This limits the use of full-reference image quality assessment metrics like SSIM and PSNR. Table II lists the no reference spatial-spectral image quality assessment metric [59] over different methods for the urban dataset. From the spectral domain, we learn features that are sensitive to noise and thus, help in understanding the nature and extent of distortion in the HSIs. These, combined with the spatial (structural and textural) attributes, help us learn quality-sensitive traits from the image. These features help frame a multivariate Gaussian model, which comes in handy in generating a final quality score for the HSIs without a reference image. A lower score signifies a better-reconstructed output image. From the table, the proposed methodology (*CompoHyDen*) performs the best, outperforming all of the other state-of-the-art methods, making it a perfect fit for the scenarios where groundtruth is unavailable.

D. Discussion

In this section, we analyze the running time of different methods, followed by sensitivity analysis of the regularization parameters λ_1 and λ_2 under different realizations of noise cases

	Cuprite	ICVL	Urban
LRTV	419.8618	354.2673	160.7258
LRTDTV	174.7828	112.8235	135.3603
NMoG	192.0058	216.6204	229.3287
LRTFDFR	24.1201	49.36	28.6529
FGSLR	4031.7641	7351.7868	**13.34**
GLF	483.8753	2054.7678	725.6723
3DlogTNN	559.2449	202.3369	287.0228
EnhancedTV	73.5208	42.8508	113.8982
L1HyMixDe	269.3137	1234.1584	13.7002
CompoHyDen	**9.78**	**31.36**	43.8530

The best values are highlighted in bold.

on the Cuprite dataset. Furthermore, convergence of the proposed methodology is also undertaken.

1) Running Time Analysis: The efficiency of any algorithm is estimated based on its running time. Table III gives an overview of the running time (in seconds) of the proposed algorithm compared with nine other methods. These results are tabulated for both the synthetic datasets (Cuprite and ICVL) as well as the real Urban dataset. On the Cuprite and ICVL datasets, the proposed method running time is 9.78 and 31.36 s, significantly outperforming all of the other methods. For example, its running time is about 27 and 40 times faster than L1HyMixDe on the Cuprite and ICVL datasets, respectively. However, for the Urban dataset, FGSLR and L1HyMixDe, with running times of 13.34 and 13.7002, respectively, outperform the proposed method (43.8530 s). Still, it outperforms 6 out of 9 methods on the Urban dataset. Pertinent to mention is that all the experiments are conducted on a PC equipped with MATLAB on the Microsoft Windows operating system. The hardware resources include an Intel i7 processor with 16 GB RAM.

2) Parameter Sensitivity Analysis: Regularization of hyperparameters can have far-reaching effects on the restoration performance of HSIs, both visually and in terms of the quantitative metrics. According to (3), λ_1 is appended to the prior $J(u)$ which in our case is a modified version of TV regularization. On the other hand, λ_2 introduces exact sparsity over the impulse noise component v. In Fig. 12, we have attempted to obtain the best values of PSNR and SSIM for different realizations of noise over the Cuprite dataset by tweaking the values of the scalars λ_1 and λ_2. Best PSNRs are obtained from cases 1, 3, 5, and 7, while best SSIMs are obtained from cases 2, 6, 8, and 9. Values of λ_1 for all the cases are varied between $1e-5$ and $1e+0.5$ while the values of λ_2 are varied between $1e-3$ and 10. The optimal values of λ_1 and λ_2 are mentioned in the caption of Fig. 12.

3) Convergence Analysis: The convergence analysis of any optimization-based image inversion problem must be studied in order to confirm its efficiency when deployed in a real-world environment. Therefore, we conducted an empirical study of the proposed methodology's convergence speed for different noise realisations on the *Cuprite* dataset. The relative change in the optimal value u_k during subsequent passages through the algorithm is shown in Fig. 13. Noise simulations are shown in
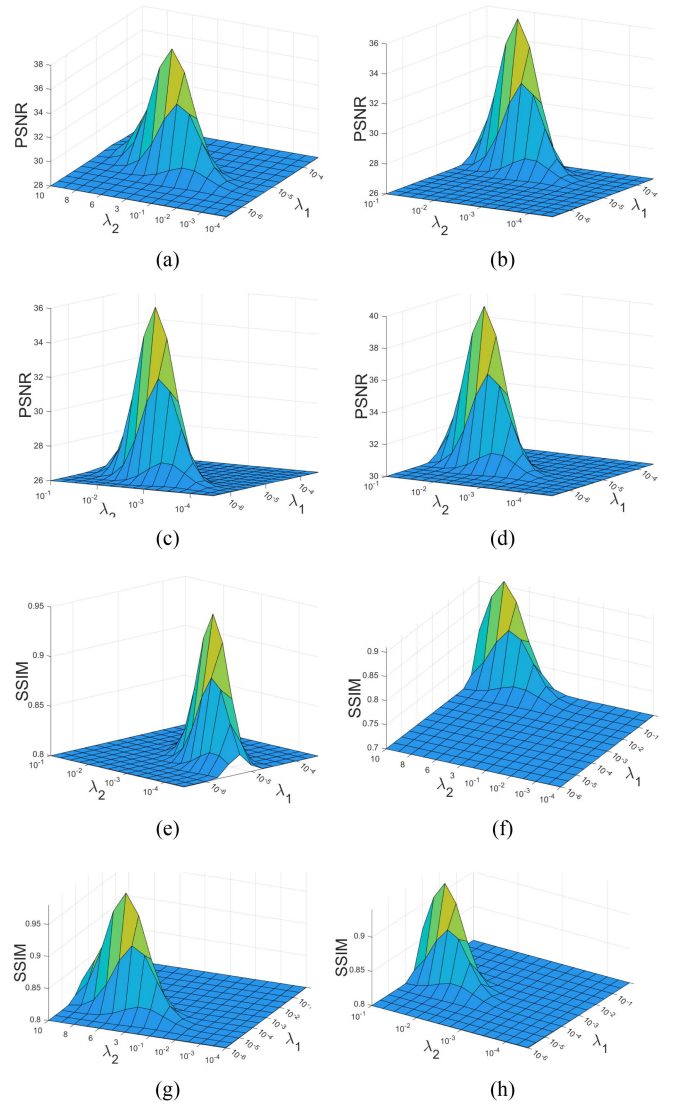

Fig. 12. Optimization of hyperparameters (λ_1, λ_2) and the corresponding values of PSNR and SSIM. Case 1: $(\lambda_1 = 10e-2, \lambda_2 = 3)$, Case 3: $(\lambda_1 = 10e-1, \lambda_2 = 6)$, Case 5: $(\lambda_1 = 10e-4, \lambda_2 = 3)$, Case 7: $(\lambda_1 = 10e-3, \lambda_2 = 6)$, Case 2: $(\lambda_1 = 10e-3, \lambda_2 = 10e-2)$, Case 6: $(\lambda_1 = 1.5, \lambda_2 = 8)$, Case 8: $(\lambda_1 = 10e-4, \lambda_2 = 6)$, Case 9: $(\lambda_1 = 10e-3, \lambda_2 = 8)$.

the figure for five different cases: cases 1, 3, 5, 7, and 9. The algorithm converges around the 40th iteration in all of the cases depicted in the figure. This demonstrates the robustness of the proposed methodology over a wide range and types of noise levels. The plot results are in direct agreement with any first order gradient-based optimization technique where there is large relative change in the optimal value during the initial iterations. This starts to stabilize as the solution starts to move towards an optimal value.

VI. CONCLUSION

This work proposes a novel approach for denoising HSIs corrupted by Gaussian noise, impulse noise, stripes, and deadlines. Considering that impulse noise is sparsely scattered throughout the spatial and spectral planes, we initially suggest a rationale for
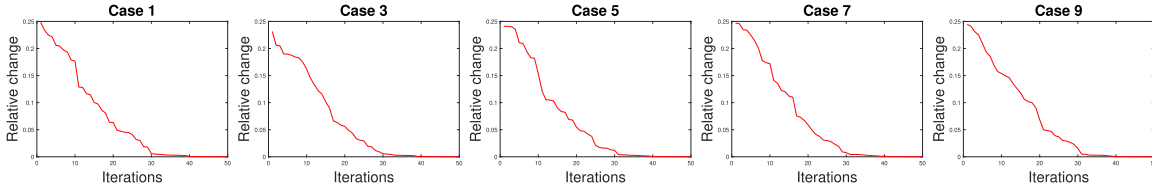
Fig. 13. Convergence analysis using relative change $(\|u_{k+1} - u_k\|_F)/\|u_k\|_F$ under optimal setting of λ_1 and λ_2 for different noise cases for *Cuprite* dataset.

using ℓ_0-norm to model the exact sparsity in the data. Since the resultant optimization problem is nonconvex and noncontinuous, the problem is reformulated by introducing an auxiliary variable. To handle the spatial and spectral similarity in the data, a nonlocal and vectorized representation of TV is used as a prior over clean estimation. Extensive results are presented to cover nine different degradation scenarios encountered in real hyperspectral data over five different spatial and spectral metrics.

Although the proposed method *(CompoHyDen)* performs well on the no-reference metric and has substantially less running time on the synthetic data than the other methods, its runtime increases on the Urban dataset. In our future endeavors, we intend to explore the effect of the sequence of noise simulation (Gaussian noise followed by impulse noise and viceversa) on the restoration quality of HSIs. Moreover, for the detection of impulse corrupted pixels, more robust and accurate methods need to be developed to achieve the perfect dichotomy of pixels set into Gaussian and impulse corrupted ones.

APPENDIX A
PROXIMAL EVALUATION OF $\ell_\infty-$NORM

The proximal operator of $\|u\|_\infty$ can be computed using Moreau decomposition [44] without resorting to estimating subgradient. Thus, the Moreau decomposition is given by

$$v = \text{prox} f(v) + \text{prox} f^*(v) \tag{28a}$$

where the convex conjugate f^* is given by

$$f^*(u) = \sup_y (u^T y - f(y)). \tag{28b}$$

When the given function is a norm, its convex conjugate is an indicator function. This is based on dual norm, i.e., for $f(u) = \|u\|_p \quad \forall p \geq 1$

$$f^*(u) = \mathbf{1}_{\|u\|_q \leq 1}(u) \text{ such that } \frac{1}{p} + \frac{1}{q} = 1. \tag{29}$$

The indicator function is given by

$$\mathbf{1}_s(u) = \begin{cases} 0, & \text{; for } u \in S \\ \infty, & \text{; for } u \notin S. \end{cases} \tag{30}$$

In our specific case when $f(u) = \|u\|_\infty$, $f^*(u) = \mathbf{1}_{\{\|u\|_1 \leq 1\}}(u)$. Further, we already know that $\text{prox} f(y) = y = \text{prox} f^*(y)$. Thus

$$\text{prox} f^*(y) = \arg\min_u \left(\mathbf{1}_{\{\|u\|\leq 1\}} + \|y - u\|_2^2 \right). \tag{31}$$

This is basically a projection on $\textrm{Ł}_1-$ball. The resultant proximal operator of $\ell_\infty-$norm is given by

$$\text{prox}_\lambda \| \cdot \|(y) = y - \lambda \text{Proj}_{\{\|\cdot\| \leq 1\}}\left(\frac{y}{\lambda}\right). \tag{32}$$

REFERENCES

[1] P. L. Vora, J. E. Farrell, J. D. Tietz, and D. H. Brainard, "Image capture: Simulation of sensor responses from hyperspectral images," *IEEE Trans. Image Process.*, vol. 10, no. 2, pp. 307–316, Feb. 2001.

[2] W. Sun, K. Ren, X. Meng, C. Xiao, G. Yang, and J. Peng, "A band divide-and-conquer multispectral and hyperspectral image fusion method," *IEEE Trans. Geosci. Remote Sens.*, vol. 60, 2021, Art. no. 5502113.

[3] G. Lu and B. Fei, "Medical hyperspectral imaging: A review," *J. Biomed. Opt.*, vol. 19, no. 1, 2014, Art. no. 010901.

[4] W. Liu and W. Lin, "Additive white Gaussian noise level estimation in SVD domain for images," *IEEE Trans. Image Process.*, vol. 22, no. 3, pp. 872–883, Mar. 2013.

[5] N. Bhosale, R. Manza, and K. Kale, "Analysis of effect of Gaussian, salt and pepper noise removal from noisy remote sensing images," in *Proc. 2nd Int. Conf. Emerg. Res. Comput., Inf., Commun. Appl.*, 2014, pp. 386–390.

[6] H. K. Aggarwal and A. Majumdar, "Mixed Gaussian and impulse denoising of hyperspectral images," in *Proc. IEEE Int. Geosci. Remote Sens. Symp.*, 2015, pp. 429–432.

[7] X. Ou, M. Wu, B. Tu, G. Zhang, and W. Li, "Multi-objective unsupervised band selection method for hyperspectral images classification," *IEEE Trans. Image Process.*, vol. 32, pp. 1952–1965, 2023.

[8] S. Henrot, J. Chanussot, and C. Jutten, "Correction to "Dynamical spectral unmixing of multitemporal hyperspectral images" [Jul. 16 3219–3232]," *IEEE Trans. Image Process.*, vol. 25, no. 9, pp. 4443–4443, Sep. 2016.

[9] Y. Li, Y. Shi, K. Wang, B. Xi, J. Li, and P. Gamba, "Target detection with unconstrained linear mixture model and hierarchical denoising autoencoder in hyperspectral imagery," *IEEE Trans. Image Process.*, vol. 31, pp. 1418–1432, 2022.

[10] H. Aetesam, S. K. Maji, and H. Yahia, "Bayesian approach in a learning-based hyperspectral image denoising framework," *IEEE Access*, vol. 9, pp. 169335–169347, 2021.

[11] H. Aetesam and S. K. Maji, "Perceptually-motivated adversarial training for deep ensemble denoising of hyperspectral images," *Remote Sens. Lett.*, vol. 13, no. 8, pp. 767–777, 2022.

[12] C. Deng, L. Li, Z. He, J. Li, and Y. Zhu, "Monte Carlo non-local means method for hyperspectral image denoising," in *Proc. IEEE Int. Geosci. Remote Sens. Symp.*, 2018, pp. 4772–4775.

[13] C. Aswathy, V. Sowmya, and K. Soman, "Hyperspectral image denoising using low pass sparse banded filter matrix for improved sparsity based classification," *Procedia Comput. Sci.*, vol. 58, pp. 26–33, 2015.

[14] C. Zhong, J. Zhang, Q. Guo, and Y. Zhang, "Improving sparse noise removal via l0-norm optimization for hyperspectral image restoration," *IEEE Geosci. Remote Sens. Lett.*, vol. 19, 2022, Art. no. 5504105.

[15] X. Kong, Y. Zhao, J. C.-W. Chan, and J. Xue, "Hyperspectral image restoration via spatial-spectral residual total variation regularized low-rank tensor decomposition," *Remote Sens.*, vol. 14, no. 3, 2022, Art. no. 511.

[16] M. Wang, Q. Wang, and J. Chanussot, "Tensor low-rank constraint and l_0 total variation for hyperspectral image mixed noise removal," *IEEE J. Sel. Topics Signal Process.*, vol. 15, no. 3, pp. 718–733, Apr. 2021.

[17] J. Peng, Q. Xie, Q. Zhao, Y. Wang, L. Yee, and D. Meng, "Enhanced 3DTV regularization and its applications on HSI denoising and compressed sensing," *IEEE Trans. Image Process.*, vol. 29, pp. 7889–7903, 2020.

[18] M. Wang, Q. Wang, J. Chanussot, and D. Hong, "$\ell_0 - \ell_1$ hybrid total variation regularization and its applications on hyperspectral image mixed noise removal and compressed sensing," *IEEE Trans. Geosci. Remote Sens.*, vol. 59, no. 9, pp. 7695–7710, Sep. 2021.

[19] L. Zhuang, X. Fu, M. K. Ng, and J. M. Bioucas-Dias, "Hyperspectral image denoising based on global and nonlocal low-rank factorizations," *IEEE Trans. Geosci. Remote Sens.*, vol. 59, no. 12, pp. 10438–10454, Dec. 2021.

[20] A. Mahmood and M. Sears, "Per-pixel noise estimation in hyperspectral images," *IEEE Geosci. Remote Sens. Lett.*, vol. 19, 2021, Art. no. 5503205.

[21] T.-X. Jiang, L. Zhuang, T.-Z. Huang, X.-L. Zhao, and J. M. Bioucas-Dias, "Adaptive hyperspectral mixed noise removal," *IEEE Trans. Geosci. Remote Sens.*, vol. 60, 2022, Art. no. 5511413.

[22] Y. Chen, X. Cao, Q. Zhao, D. Meng, and Z. Xu, "Denoising hyperspectral image with non-iid noise structure," *IEEE Trans. Cybern.*, vol. 48, no. 3, pp. 1054–1066, Mar. 2018.

[23] G. Yuan and B. Ghanem, "ℓ_0 TV: A sparse optimization method for impulse noise image restoration," *IEEE Trans. Pattern Anal. Mach. Intell.*, vol. 41, no. 2, pp. 352–364, Feb. 2019.

[24] H. Aetesam, S. K. Maji, and J. Boulanger, "Image enhancement under Gaussian impulse noise for satellite and medical applications," in *Handbook of Research on Computer Vision and Image Processing in the Deep Learning Era*, Hershey, Pennsylvania, USA: IGI Global, 2023, pp. 309–342.

[25] T. Huang, W. Dong, X. Xie, G. Shi, and X. Bai, "Mixed noise removal via Laplacian scale mixture modeling and nonlocal low-rank approximation," *IEEE Trans. Image Process.*, vol. 26, no. 7, pp. 3171–3186, Jul. 2017.

[26] H. Aetesam, K. Poonam, and S. K. Maji, "A mixed-norm fidelity model for hyperspectral image denoising under Gaussian-impulse noise," in *Proc. Int. Conf. Inf. Technol.*, 2019, pp. 137–142.

[27] H. Aetesam, S. K. Maji, and J. Boulanger, "A two-phase splitting approach for the removal of Gaussian-impulse noise from hyperspectral images," in *Proc. Int. Conf. Comput. Vis. Image Process.*, 2020, pp. 179–190.

[28] H. Zhang, W. He, L. Zhang, H. Shen, and Q. Yuan, "Hyperspectral image restoration using low-rank matrix recovery," *IEEE Trans. Geosci. Remote Sens.*, vol. 52, no. 8, pp. 4729–4743, Aug. 2014.

[29] A. B. Hamza, H. Krim, and G. B. Unal, "Unifying probabilistic and variational estimation," *IEEE Signal Process. Mag.*, vol. 19, no. 5, pp. 37–47, Sep. 2002.

[30] P. J. Huber et al., "The behavior of maximum likelihood estimates under nonstandard conditions," in *Proc. 5th Berkeley Symp. Math. Statist. Probability*, 1967, vol. 1, pp. 221–233.

[31] C. Zeng, C. Wu, and R. Jia, "Non-Lipschitz models for image restoration with impulse noise removal," *SIAM J. Imag. Sci.*, vol. 12, no. 1, pp. 420–458, 2019.

[32] T. Chen and H. R. Wu, "Adaptive impulse detection using center-weighted median filters," *IEEE Signal Process. Lett.*, vol. 8, no. 1, pp. 1–3, Jan. 2001.

[33] L. I. Rudin, S. Osher, and E. Fatemi, "Nonlinear total variation based noise removal algorithms," *Physica D: Nonlinear Phenomena*, vol. 60, no. 1–4, pp. 259–268, 1992.

[34] A. Buades, B. Coll, and J.-M. Morel, "A non-local algorithm for image denoising," in *Proc. IEEE Comput. Soc. Conf. Comput. Vis. Pattern Recognit.*, vol. 2, 2005, pp. 60–65.

[35] G. Gilboa and S. Osher, "Nonlocal operators with applications to image processing," *Multiscale Model. Simul.*, vol. 7, no. 3, pp. 1005–1028, 2009.

[36] P. Rodriguez and B. Wohlberg, "A generalized vector-valued total variation algorithm," in *Proc. IEEE 16th Int. Conf. Image Process.*, 2009, pp. 1309–1312.

[37] P. Blomgren and T. F. Chan, "Color TV: Total variation methods for restoration of vector-valued images," *IEEE Trans. Image Process.*, vol. 7, no. 3, pp. 304–309, Mar. 1998.

[38] P. Rodríguez and B. Wohlberg, "Efficient minimization method for a generalized total variation functional," *IEEE Trans. Image Process.*, vol. 18, no. 2, pp. 322–332, Feb. 2009.

[39] P. Liu, J. Liu, and L. Xiao, "A unified pansharpening method with structure tensor driven spatial consistency and deep plug-and-play priors," *IEEE Trans. Geosci. Remote Sens.*, vol. 60, 2022, Art. no. 5413314.

[40] L. Yang, J. Xu, and L. Xiao, "Hyperspectral image denoising with collaborative total variation and low rank regularization," in *Proc. IEEE Int. Geosci. Remote Sens. Symp.*, 2021, pp. 4139–4142.

[41] Q. Ge et al., "Structure-based low-rank model with graph nuclear norm regularization for noise removal," *IEEE Trans. Image Process.*, vol. 26, no. 7, pp. 3098–3112, 2017.

[42] T. Goldstein, M. Li, and X. Yuan, "Adaptive primal-dual splitting methods for statistical learning and image processing," in *Proc. Int. Conf. Adv. Neural Inf. Process. Syst.*, 2015, vol. 28, pp. 2089–2097.

[43] H. Aetesam, K. Poonam, and S. K. Maji, "Proximal approach to denoising hyperspectral images under mixed-noise model," *IET Image Process.*, vol. 14, no. 14, pp. 3366–3372, 2020.

[44] N. Parikh et al., "Proximal algorithms," *Found. Trends Optim.*, vol. 1, no. 3, pp. 127–239, 2014.

[45] X. Liu, X. Lu, H. Shen, Q. Yuan, Y. Jiao, and L. Zhang, "Stripe noise separation and removal in remote sensing images by consideration of the global sparsity and local variational properties," *IEEE Trans. Geosci. Remote Sens.*, vol. 54, no. 5, pp. 3049–3060, May 2016.

[46] Y. Chang, L. Yan, H. Fang, and C. Luo, "Anisotropic spectral-spatial total variation model for multispectral remote sensing image destriping," *IEEE Trans. Image Process.*, vol. 24, no. 6, pp. 1852–1866, Jun. 2015.

[47] W. He, H. Zhang, L. Zhang, and H. Shen, "Total-variation-regularized low-rank matrix factorization for hyperspectral image restoration," *IEEE Trans. Geosci. Remote Sens.*, vol. 54, no. 1, pp. 178–188, Jan. 2016.

[48] Y. Wang, J. Peng, Q. Zhao, Y. Leung, X.-L. Zhao, and D. Meng, "Hyperspectral image restoration via total variation regularized low-rank tensor decomposition," *IEEE J. Sel. Topics Appl. Earth Observ. Remote Sens.*, vol. 11, no. 4, pp. 1227–1243, Apr. 2017.

[49] Y.-B. Zheng, T.-Z. Huang, X.-L. Zhao, Y. Chen, and W. He, "Double-factor-regularized low-rank tensor factorization for mixed noise removal in hyperspectral image," *IEEE Trans. Geosci. Remote Sens.*, vol. 58, no. 12, pp. 8450–8464, Dec. 2020.

[50] Y. Chen, T.-Z. Huang, W. He, X.-L. Zhao, H. Zhang, and J. Zeng, "Hyperspectral image denoising using factor group sparsity-regularized nonconvex low-rank approximation," *IEEE Trans. Geosci. Remote Sens.*, vol. 60, 2022, Art. no. 5515516.

[51] Q. Ran, W. Li, Q. Du, and C. Yang, "Hyperspectral image classification for mapping agricultural tillage practices," *J. Appl. Remote Sens.*, vol. 9, no. 1, 2015, Art. no. 097298.

[52] Y.-B. Zheng, T.-Z. Huang, X.-L. Zhao, T.-X. Jiang, T.-H. Ma, and T.-Y. Ji, "Mixed noise removal in hyperspectral image via low-fibered-rank regularization," *IEEE Trans. Geosci. Remote Sens.*, vol. 58, no. 1, pp. 734–749, Jan. 2019.

[53] Y. Yang, J. Zheng, S. Chen, and M. Zhang, "Hyperspectral image restoration via local low-rank matrix recovery and Moreau-enhanced total variation," *IEEE Geosci. Remote Sens. Lett.*, vol. 17, no. 6, pp. 1037–1041, Jun. 2020.

[54] L. Zhuang and M. K. Ng, "Hyperspectral mixed noise removal by ℓ_1-norm-based subspace representation," *IEEE J. Sel. Topics Appl. Earth Observ. Remote Sens.*, vol. 13, pp. 1143–1157, 2020.

[55] Z. Wang, A. C. Bovik, H. R. Sheikh, and E. P. Simoncelli, "Image quality assessment: From error visibility to structural similarity," *IEEE Trans. Image Process.*, vol. 13, no. 4, pp. 600–612, Apr. 2004.

[56] L. Zhang, L. Zhang, X. Mou, and D. Zhang, "FSIM: A feature similarity index for image quality assessment," *IEEE Trans. Image Process.*, vol. 20, no. 8, pp. 2378–2386, Aug. 2011.

[57] R. H. Yuhas, A. F. Goetz, and J. W. Boardman, "Discrimination among semi-arid landscape endmembers using the spectral angle mapper (SAM) algorithm," in *Proc. JPL, Summaries 3rd Annu., JPL Airborne Geosci. Workshop*, Pasadena, California: Jet Propulsion Laboratory, Jun. 1992, vol. 1.

[58] D. Renza, E. Martinez, and A. Arquero, "A new approach to change detection in multispectral images by means of ERGAS index," *IEEE Geosci. Remote Sens. Lett.*, vol. 10, no. 1, pp. 76–80, Jan. 2013.

[59] J. Yang, Y.-Q. Zhao, C. Yi, and J. C.-W. Chan, "No-reference hyperspectral image quality assessment via quality-sensitive features learning," *Remote Sens.*, vol. 9, no. 4, 2017, Art. no. 305.

Hazique Aetesam received the B.Tech. degree in information technology from Jamia Hamdard, New Delhi, India, in 2013, the M.Tech. degree in computer science and engineering (CSE) from the Birla Institute of Technology Mesra, Mesra, India, in 2016, and the Ph.D. degree in CSE from the Indian Institute of Technology Patna, India, in 2022.

He focused on image restoration under Gaussian and impulse noise using model and data-driven approaches. He is currently an Assistant Professor with the Department of CSE, Birla Institute of Technology Mesra. He is working on the low-level computer vision problems pertaining to hyperspectral imaging and magnetic resonance imaging domains. His current research interests include the amalgamation of model and data-driven approaches in different types of image related inverse problems in different application domains.

Abdul Wasi received the bachelor in engineering (B.E.) degree in computer science and engineering from Chandigarh University, Mohali, India, in 2023.

He is currently a Research Associate with the Centre for Visual Information Technology, Indian International Institute of Indian Technology, Hyderabad, India. His research interests include computational photography, remote sensing, and video understanding.

Sonal Sharma received the bachelor's degree in information technology (IT) from Engineering College Kota, Kota, India, in 2006, the master's degree in computer science and engineering (CSE) from Rajasthan Technical University, Kota, in 2013, and the Ph.D. degree in CSE from Career Point University, Kota, in 2017.

She has more than 15 years of teaching and research experience. She is currently the Head and Associate Professor of cloud technology in mobile application and information security with the Department of Computer Science and Engineering, Jain University (Deemed-to-be University), Bangalore, India. She trained the students at undergraduate and postgraduate levels, and research scholars in domains not limiting to cloud computing and security, cybersecurity, and image processing domains. She has authored or coauthored more than 25 papers in journals and three books. Her research interests include artificial intelligence, cloud computing, cybersecurity, and nature-inspired algorithms.

Dr. Sharma was the recipient of many awards for her research activities including Asian Award for Young Professor 2023, India Prime Icon 2022, and Best Academician from IFST 2020. She has presented and published research papers in various conferences of national and international repute.